Eole Code Validation Report

Structural response and code validation of the Wind Harvester 3.1 VAWT

Contents

List of Figures

1   Background

Straight-bladed vertical axis wind turbines (VAWTs) have been under development for some time and have shared with their curved-blade counterparts a range of engineering and economic challenges [xx, xx, xx]. Those challenges have included fatigue loading and avoiding resonant conditions, but the attractions of the H-shape are clear: simple blade construction, a nacelle near ground level, and aerodynamic efficiency.

Wind Harvest International (WHI) is developing a straight-bladed VAWT rated at approximately 70 kW which can be used to augment existing wind farms by being placed in the "understory". It can also be installed in rows and benefit from the performance augmentation that has been demonstrated to occur [xx].

A prototype, the version 3.1, has been installed at the UL test site in Texas [xx] and instrumented to allow confirmation of the predictions made for the turbine. Those predictions include the power performance and also the structural response in the main members of the rotor. Figure XX shows the turbine and the locations of the strain gauges.
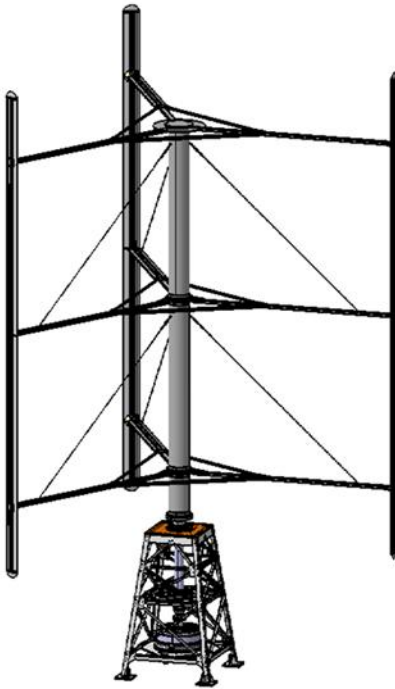
Figure 1. The WHI v31

The rotor is connected to a direct drive permanent magnet generator which can accommodate variable speed operation. The turbine has been run in a number of fixed-speed as well as variable speed mode.

2   Objectives

This report has the following objectives:

- To describe the modeling of the turbine operation and prediction of structural loads.
- To present the electrical performance of the turbine in the form of power coefficient vs. tip speed ratio.
- To compare the performance with predictions.
- To present the harmonic response from key components and compare with predictions.
- To present fatigue loads, in the form of rainflow counting cycles, and compare with predictions.
- To draw conclusions on the agreement of predictions with field data.
- To evaluate the reliability of the modeling procedure.

3   The Test Site

The WHI 3.1 prototype was installed at the UL wind test site near Amarillo, Texas, in 2021. The test site and location of the turbine and of the anemometers is shown in Figure 2.
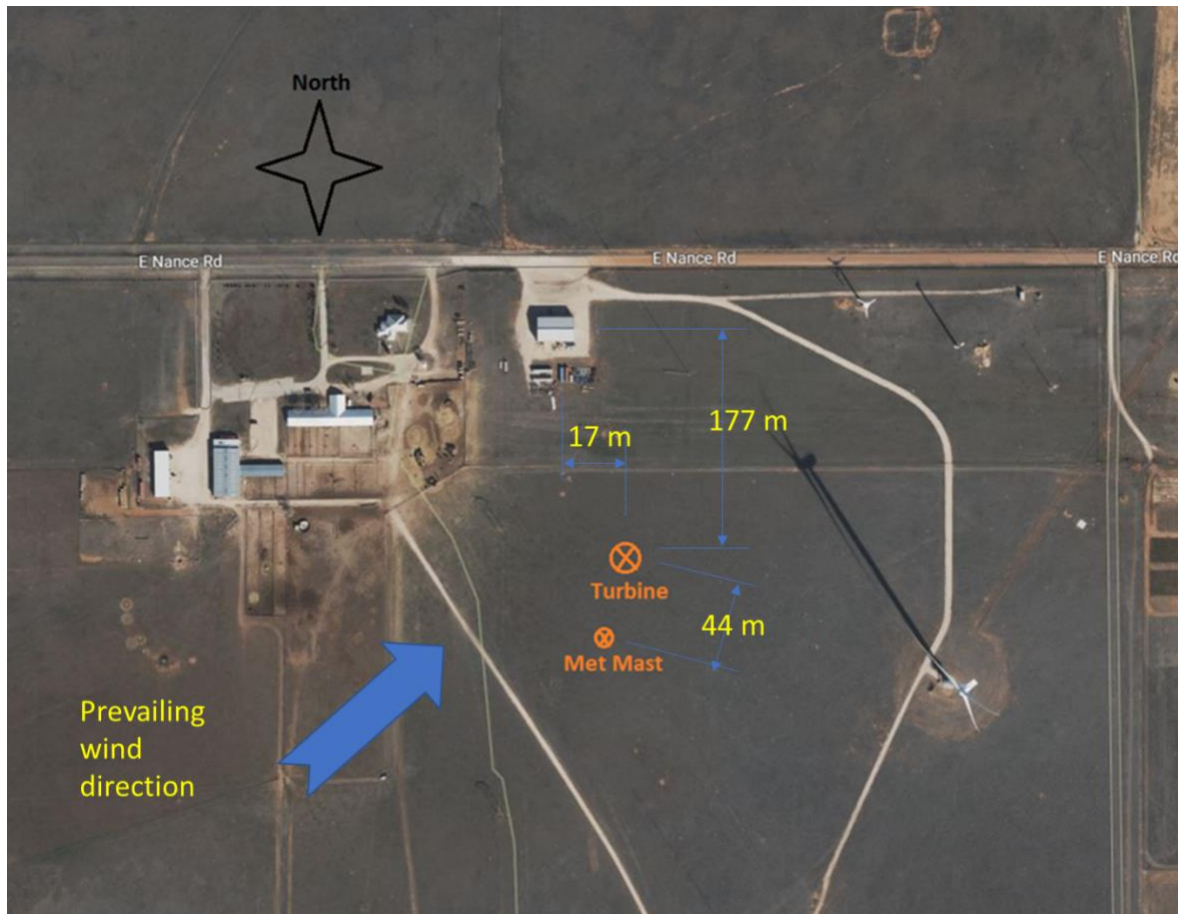
Figure 2. layout of turbine at UL test site

Figure 3 shows the location of the sensors used in this report. All gauges were backed up with duplicates in case of failure. The term "in-plane" refers to bending action within the plane containing the blade and the arms. In the HAWT industry this would be labelled "flapwise" bending in the blades.
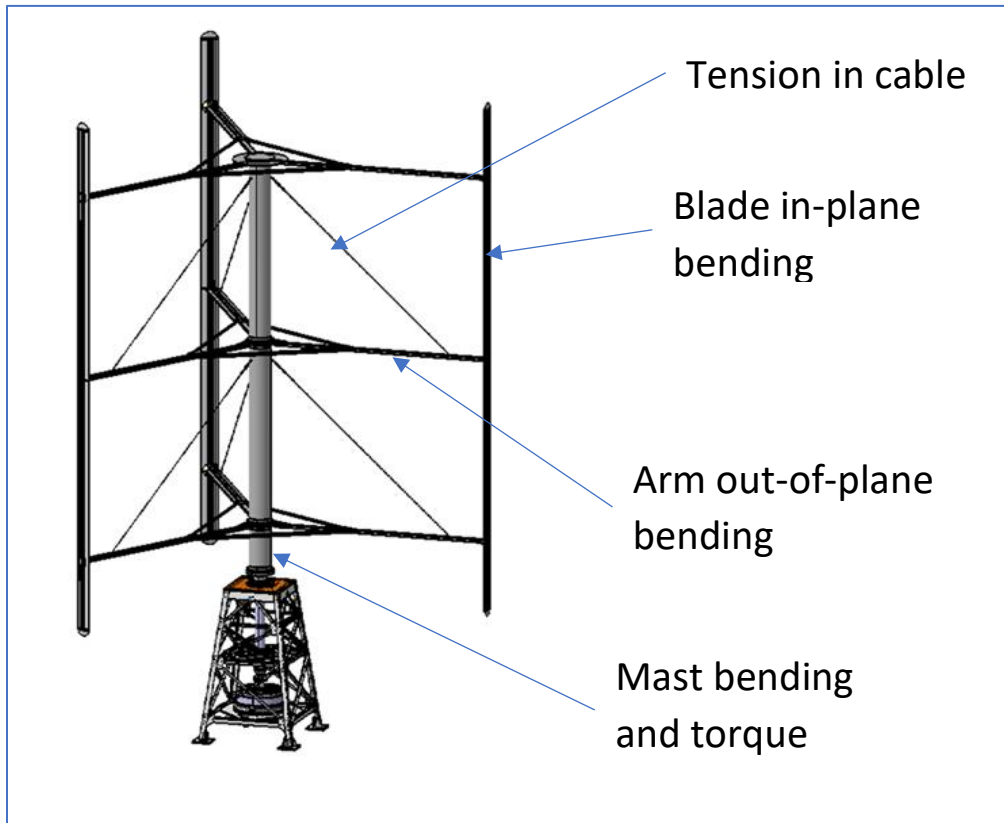
Figure 3. location of sensor used in this report

The sensors were calibrated to output the bending moment by noting the section modulus of the members to which they were attached. The two anemometers on the met mast were positioned at heights equivalent to the top and bottom of the rotor blades (18.0 m and 4.0 respectively). All wind speeds referenced in this document are the averages from the two anemometers.

4 Aeroelastic modeling

Modern aeroelastic codes for horizontal axis wind turbines (HAWTs) commonly use a time integration approach which can simulate operation in turbulent flow and various transients. Such codes are not readily available to the VAWT industry especially to companies of limited financial means. WHI has made use of codes that were developed some time ago for the frequency response of VAWTs in steady winds.

4.1 The Eole suite of codes

The work at Sandia National Laboratories on the structural dynamics of the Darrieus rotor took place in the 1980s when the capacity of computers was only a fraction of their current speed and memory [1, 2]. In the 1990s, in response to the availability of personal computers, albeit of limited capacity, a suite of codes (the EOLE suite [3, 4]) was developed to carry out the extraction of the complex operating frequencies and the response at harmonic frequencies to a constant wind flow. Both of these codes made

use of the real natural mode shapes of the stationary rotor as generalized coordinates, thereby reducing the size of the matrices involved. Flowcharts for the two codes are shown in Figure 4.
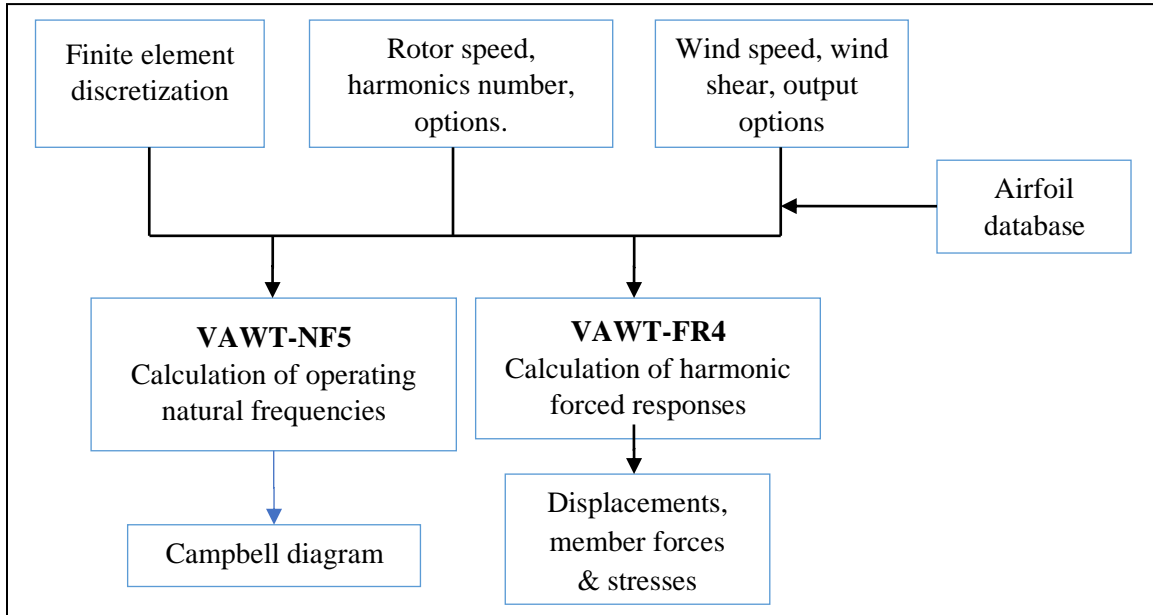
Figure 4.The Eole suite of VAWT codes

Finite element model of rotor → Real eigenvalue & vector extraction by sub-space iteration

Real eigenvectors

Operating rpm → Add pretensioning and rotational softening to stiffness. Create Coriolis matrix → Reduce system matrices

Extract complex modes and frequencies with Upper Hessenberg algorithm

Campbell diagram of natural frequencies vs. rpm

Complex modes in terms of real modes

Figure 5. Extraction of operating natural frequencies and mode shapes

In the VAWT-NF code, the natural frequencies and mode shapes of the stationary rotor are first extracted and used as generalized coordinates for the remaining operations. These include the extraction of the complex natural modes of the rotating system, which is a conservative, gyroscopic one and is done using the upper Hessenberg algorithm. A flowchart of the code is shown in Figure 5. Comparisons between the natural frequency predictions made by the VAWT-NF code and those obtained by SNL's own NASTRAN-based codes have been very good.

The VAWT-FR4 code uses a similar approach to reducing the size of the system matrices, by adopting the real eigenvectors of the stationary turbine as generalized coordinates for both the aerodynamic loads and for the structural response at the harmonic frequencies. The code carries out a forced response analysis at each of the rotor speed harmonic frequencies (1P, 2P, etc.). This is valid in a steady flow state and, since VAWTs are dominated by the harmonic loads even in the presence of turbulence, it is also more generally valid. A flowchart for this code is shown in **Error! Reference source not found.**
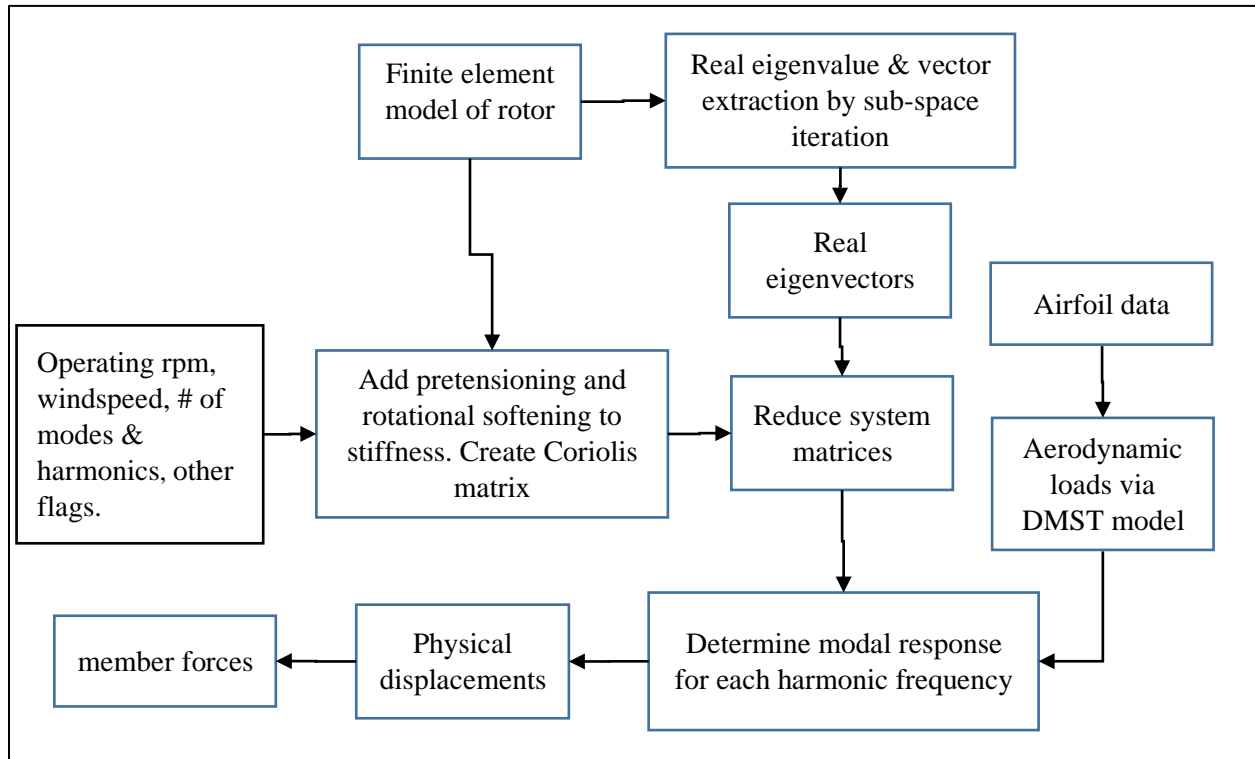
Figure 6. FR4 code for frequency response and member forces

4.2 Critical resonance

The dependency of the operating natural frequencies with rotor speed were extracted with the use of the Eole NF5 code and are shown in Figure 7 (. The determination of which of the many crossings of the harmonic loading with the natural frequencies is critical and may lead to resonance can be done by applying the FR4 code at a range of rotor speeds. The only critical crossing was predicted to be at 27 rpm when the first tilt mode crosses the 2P excitation. This was consistent with the investigation reported in [5].
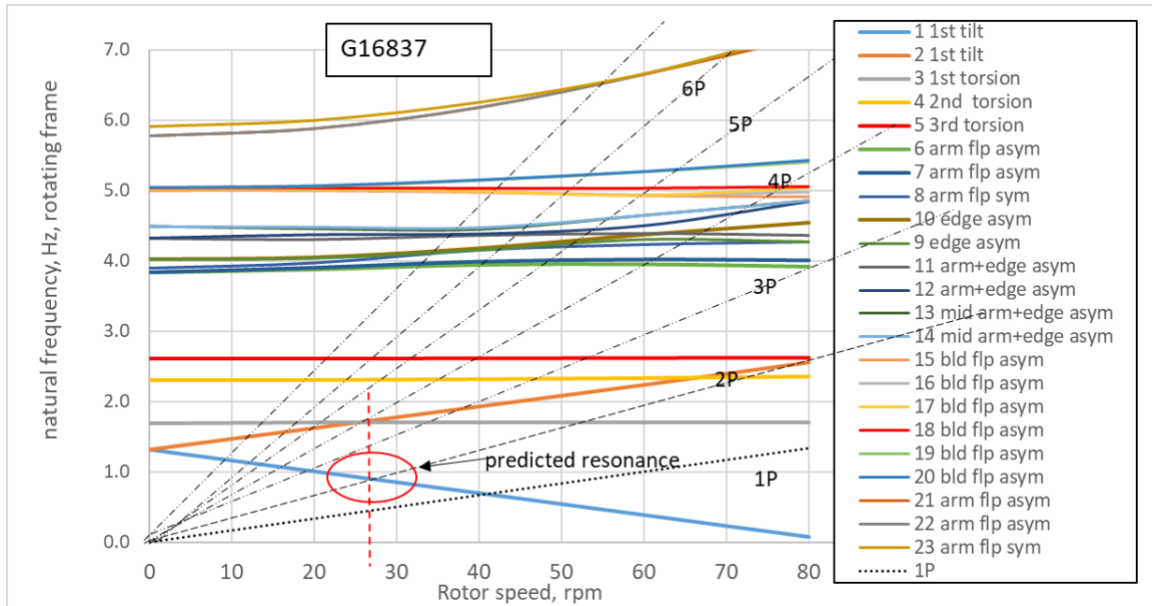
Figure 7. Operating natural frequencies vs. rpm (Campbell diagram)

The shape of the first tilt mode of the stationary rotor is shown in Figure 8. This mode is one that is affected by the rotating frame and bifurcates into two modes as the rpm increases.
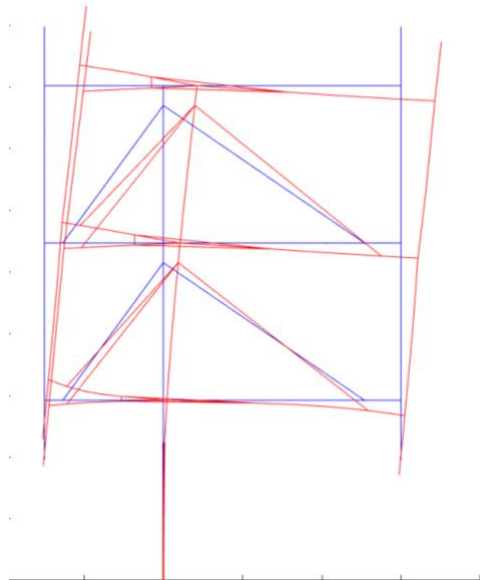
Figure 8. First tilt mode of stationary rotor

5   Data Collected

5.1   Program of data collection

As well as operating the turbine in variable speed mode, it was also operated at a number of fixed speeds at a range of wind speeds. In this way, operation at a range of tip speed ratios (ratio of tip speed / ambient wind speed) was obtained.

6   Results

6.1   Stationary rotor fundamental natural frequency

A cable was attached to the top of the mast and an impulse was applied by hand. The resulting mast bending signal is shown in Figure 9. From this the natural frequency was determined to be 1.25 Hz which is in close agreement with the Campbell diagram, Figure 7,. The modal damping ratio is a little more than 1%.
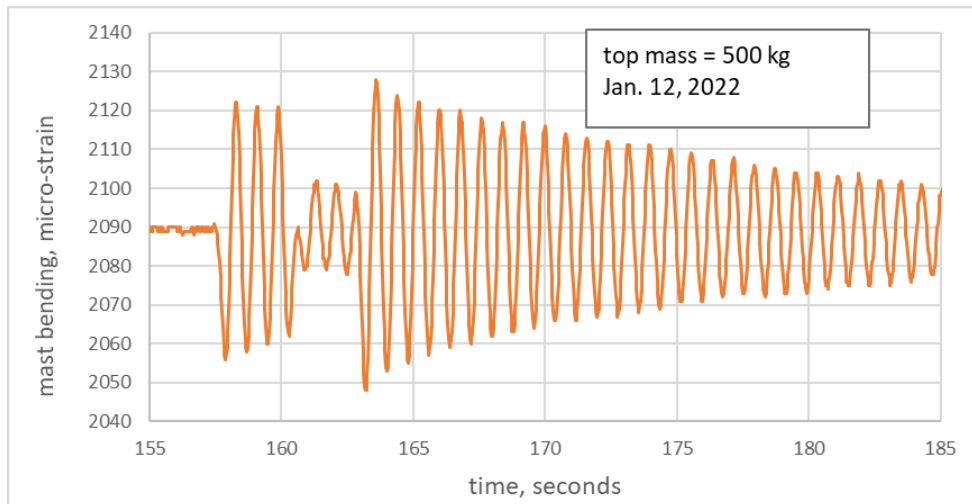
Figure 9. Mast bending following impulse to stationary rotor

6.2   Critical rpm

Figure 10 shows the mast bending as the rotor speed was decreased from 50 to zero rpm. Likewise Figure 11shows the same resonance as the rotor speed was increased. These two figures suggest a resonance at about 25 rpm which agrees with the Eole NF5 prediction (see Figure 7).
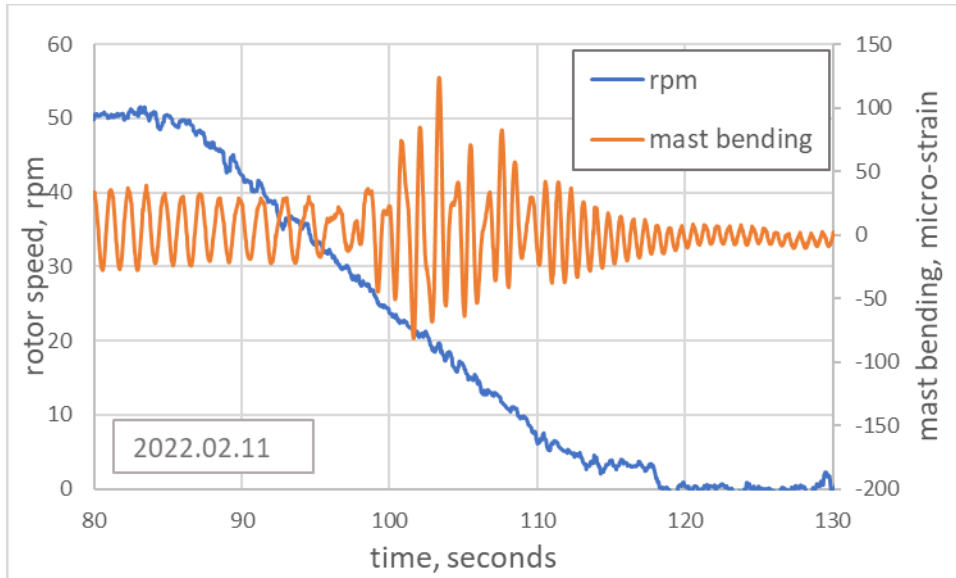
Figure 10. Resonance in rotor during braking
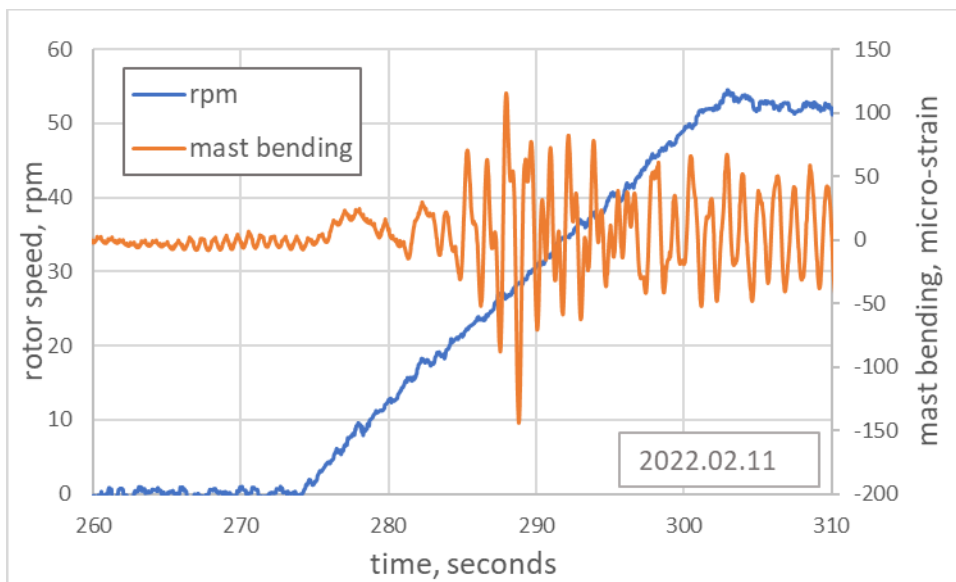
Figure 11. Mast bending resonance during motoring up

The other sensors did not indicate any resonances in the speed range of zero to 50 rpm. These results are confirmation of the accuracy of the NF5 code and of the ability of the FR4 code to identify the critical crossings [5].

6.3 Harmonic responses

By its basic aerodynamics, the loading on a VAWT is largely periodic at multiples of the rotor speed and the effect of turbulence on fatigue loads is not as strong as its effect on HAWTs [6, 7]. Therefore, the

validation of the design codes can be carried out by comparing the amplitudes of the measured harmonics with the corresponding predicted values.

This was done at a range of tip speed ratios using data from three of the sensors: lower mast bending, blade in-plane bending, and arm out-of-plane bending (see **Error! Reference source not found.**). These results are shown in a number of figures below as a ratio of measured/predicted values. A ratio of 1.0, therefore, indicates perfect agreement while values lower than 1.0 indicate measured loads that were lower than predicted.

6.4   Mast bending

6.4.1   Mast bending FFT

A typical FFT (Fast Fourier Transform) of the field data from the mast bending sensors at 65 rpm is shown in Figure 12 . As expected, the response is dominated by the 1P harmonic with some 2P response.
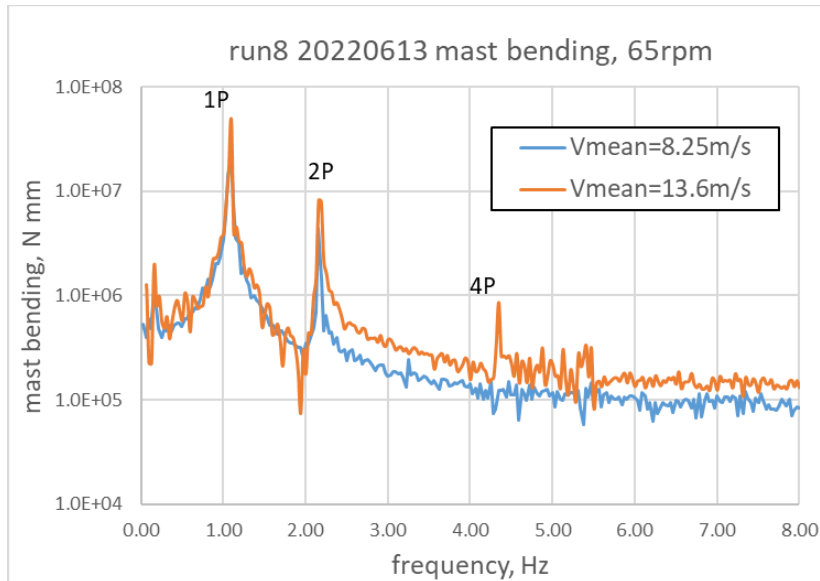
Figure 12. Typical FFTs from mast bending, 65 rpm

A similar pair of FFTs for mast bending at 46 rpm is shown in Figure 13 which shows the expected harmonic responses at 1P and 2P. It also includes a peak at 2.8 Hz which Figure 7 shows corresponds to the crossing with one of the first tilt modes.
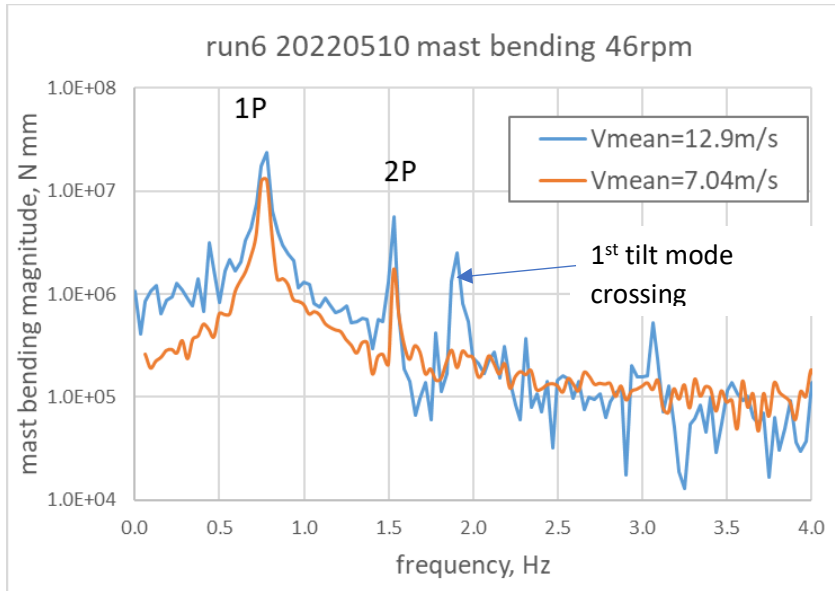
Figure 13. Typical FFTs for mast bending, 46 rpm

Another FFT of mast bending, at 35 rpm, is shown in Figure 14 which includes a 3P peak as well as 1P and 2P. Although the wind speeds were low, the tip speed ratios were also low due to the low tip speed.
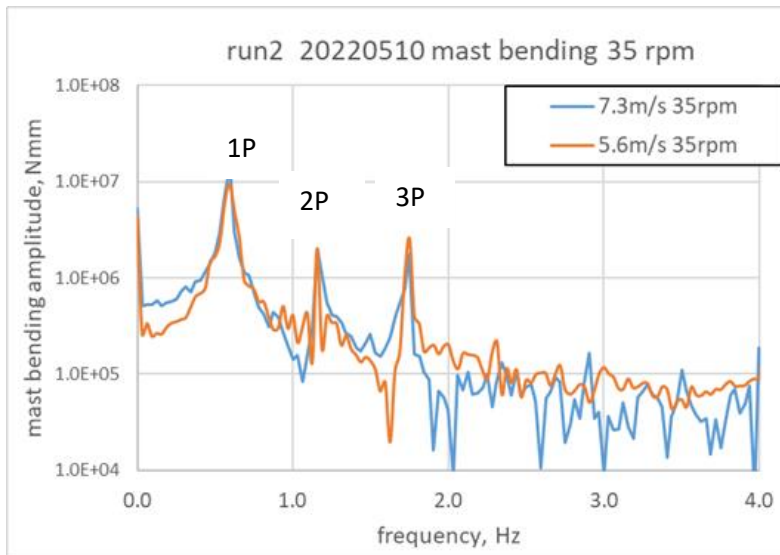
Figure 14. Typical mast bending FFT, 35 rpm

6.4.2   Harmonic response, mast bending

FR4 simulations were carried out for the range of conditions (rotor speed and mean wind speed) corresponding to the field data. The air density for all simulations was set at1.05 kg/m^3 which was estimated to be typical of the test site. The ratio of measured to predicted 1P magnitudes for a range of tip speed ratios is shown in Figure 15 together with a plot of bending moment vs. tip speed multiplied by the wind speed. The latter may be regarded as a measure of the angle of attack, (wind speed)/(tip speed), multiplied by the square of the tip speed, both of which vary linearly with aerodynamic forces. It shows excellent agreement between the measured and predicted 1P values in both plots.
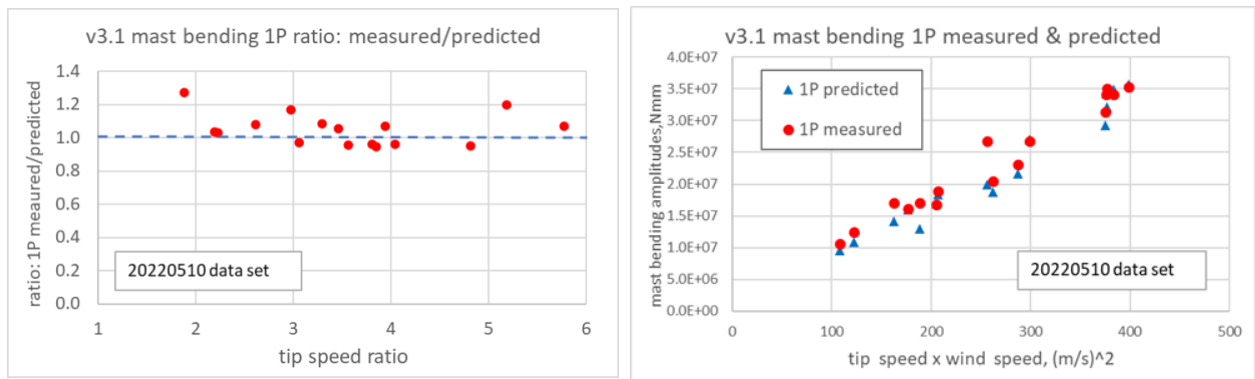
Figure 15. Values and ratio of 1P measured & predicted mast bending

Figure 16 shows the similar ratio and bending moment for the 2P response where the measured values are consistently less than the predicted values.
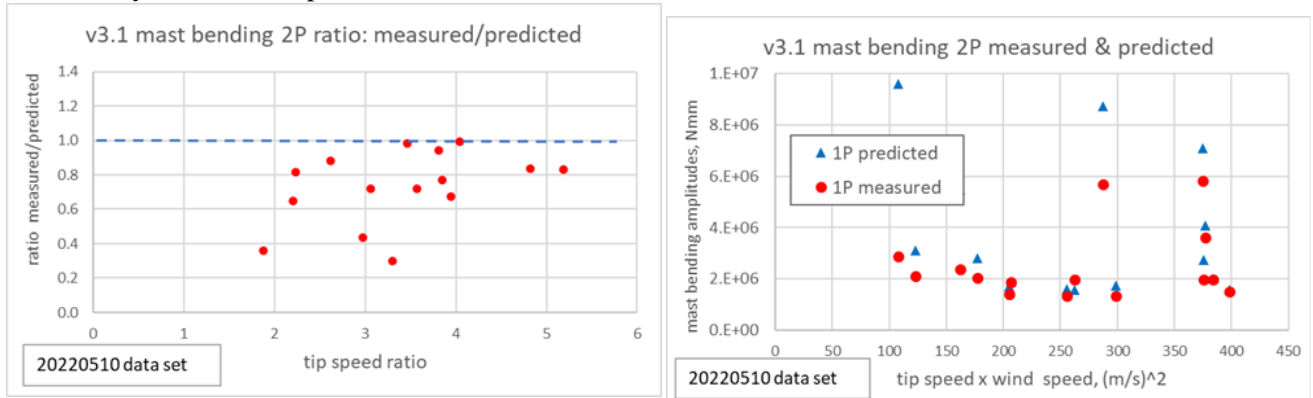
Figure 16. Values and ratio of 2P measured & predicted mast bending

The mast bending at 3P is low and is not shown here but 4P and 5P are more significant and are shown below in Figure 18 and Figure 17 .
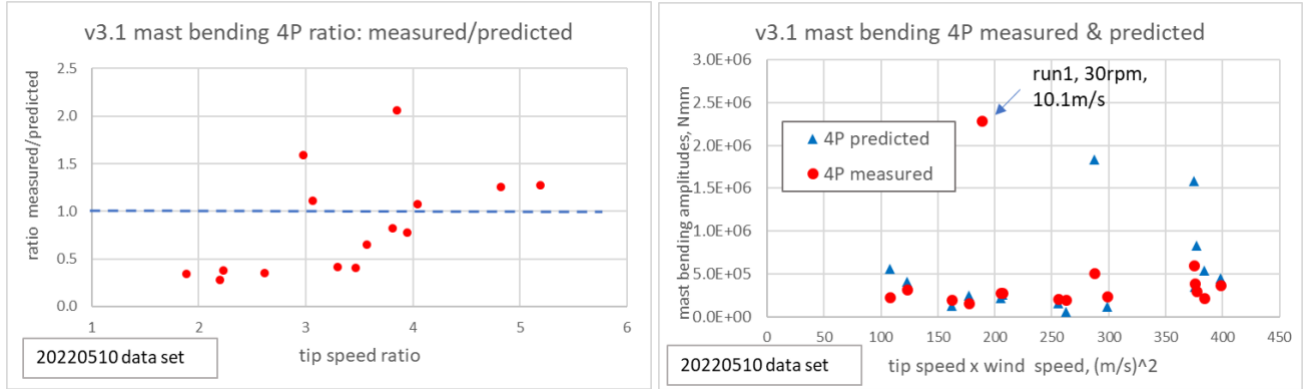
Figure 18. Ratio and values of 4P measured & predicted mast bending
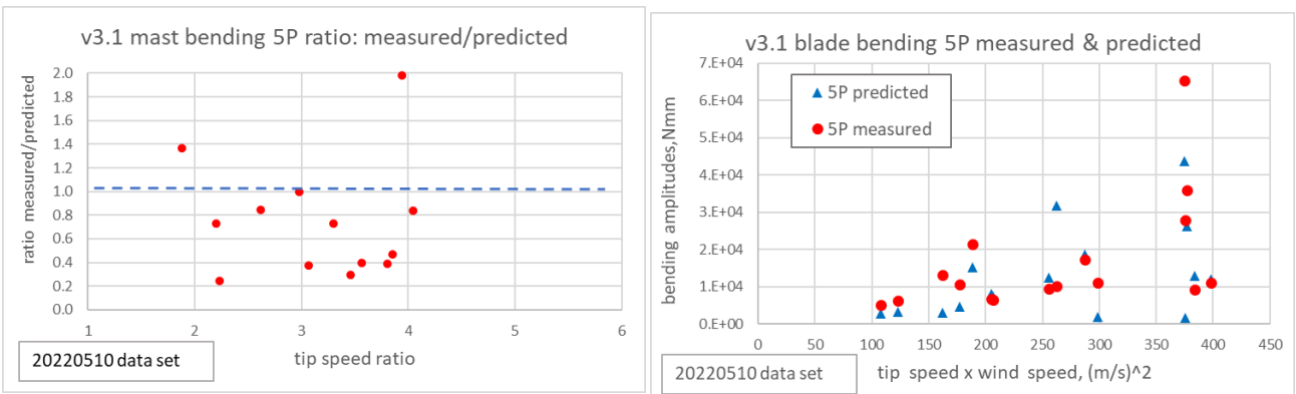
Figure 17. Values and ratio of 5P measured & predicted mast bending

6.5   Mast torque

A typical FFT from the mast torque sensor is shown in Figure 19 and Figure 20.
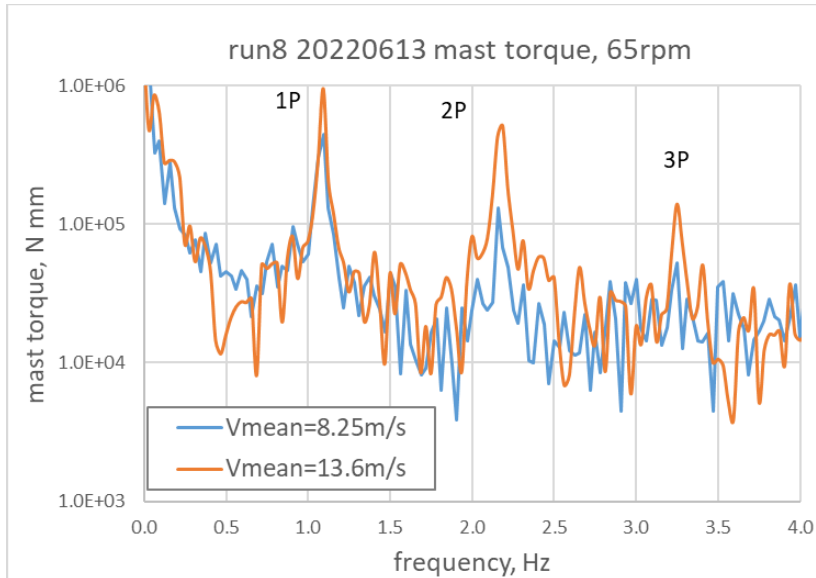
Figure 19. Typical FFT from mast torque sensor, 65 rpm
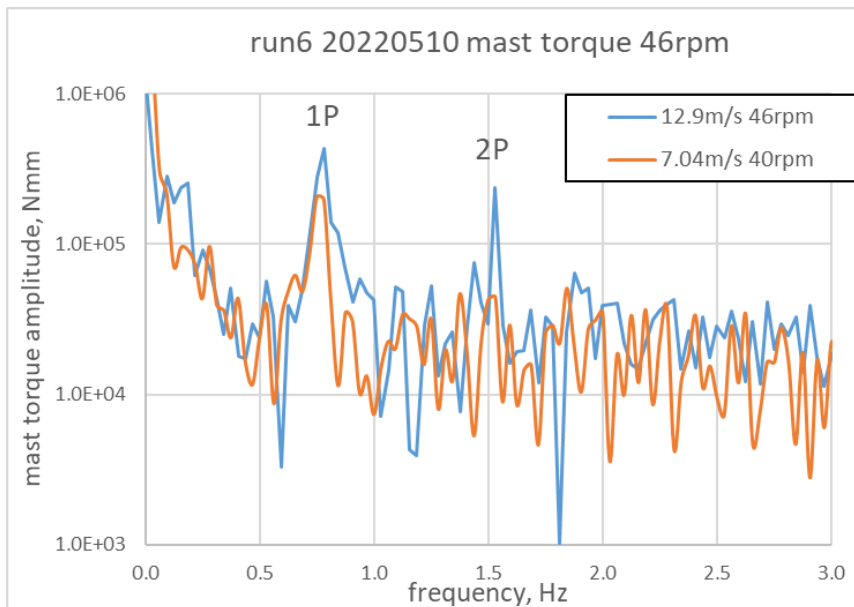
Figure 20. Typical FFT from mast torque sensor, 46 rpm

The 1P and 2P peaks are not expected although some peak at 3P is expected. It is possible that the strain gauges were not perfectly orientated at ±45° which would lead to some sensitivity to bending in the mast. It is noted that the magnitude of the 1P peak in the torque signal is approximately two decades smaller than the corresponding peak in the mast bending signal.

There are no peaks in the FFT that might indicate a possible torsional resonance.

6.6   Blade bending

6.6.1   Blade bending FFT

A typical FFT from the blade bending sensor is shown below in Figure 21.
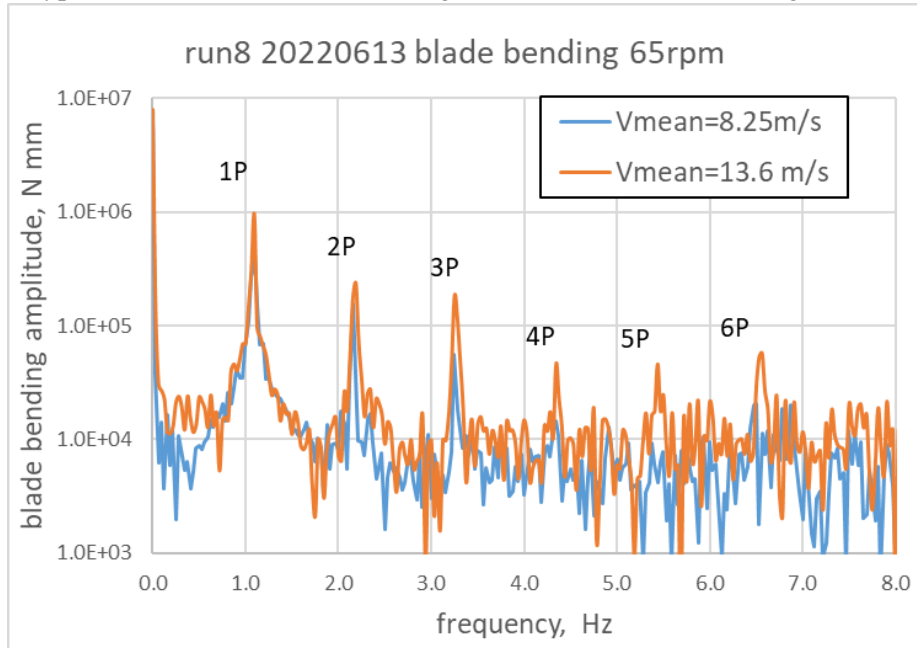
Figure 21. Typical FFT from blade bending sensor at 65 rpm.

The corresponding FFT at 46 rpm is shown in Figure 22. At both rotor speeds there is considerable response at the higher harmonics (above 3P), mainly when the wind speed is high enough to cause stall on the blades. The 4P peak is largely absent from the 46 rpm record suggesting that it may be combined with a resonance at 65 rpm.
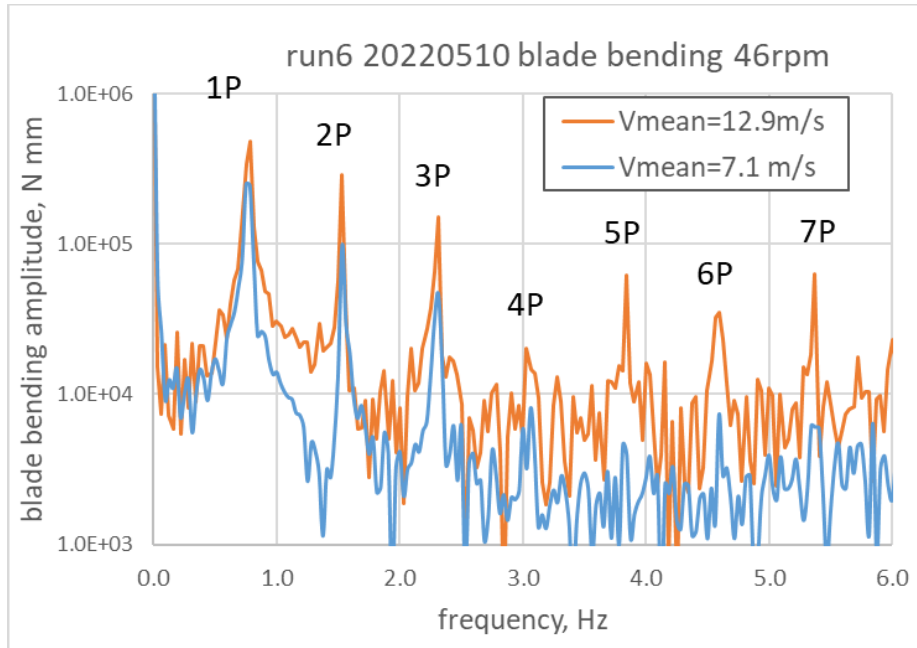
Figure 22. Typical FFT from blade bending at 46 rpm

6.6.2 Blade bending harmonics

The ratio of measured to predicted amplitudes of the dominant 1P bending in the blade over a range of tip speed ratios is shown in Figure 23. The measured values are consistently slightly lower (by 10-20%) than predicted values. One possible explanation is that downwind shadow played a greater role in those conditions. It should be noted that, although it was investigated later in the project, downwind shadow from the central mast was not incorporated into the FR4 model for these results.
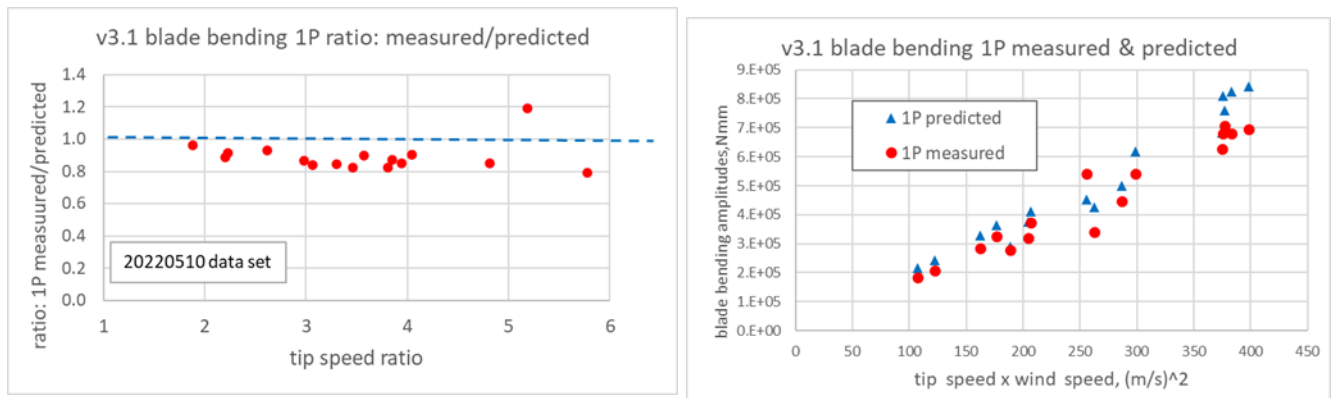
Figure 23. Values and ratios of 1P measured & predicted blade bending

The corresponding plot for 2P ratio and amplitudes is shown in Figure 24. The plot indicates that at high tip speed ratios, the measured values are greater than predicted. This quantity can be considered a measure of the difference between the aerodynamic lift on the upwind blade compared with the lift on the downwind blade.

19
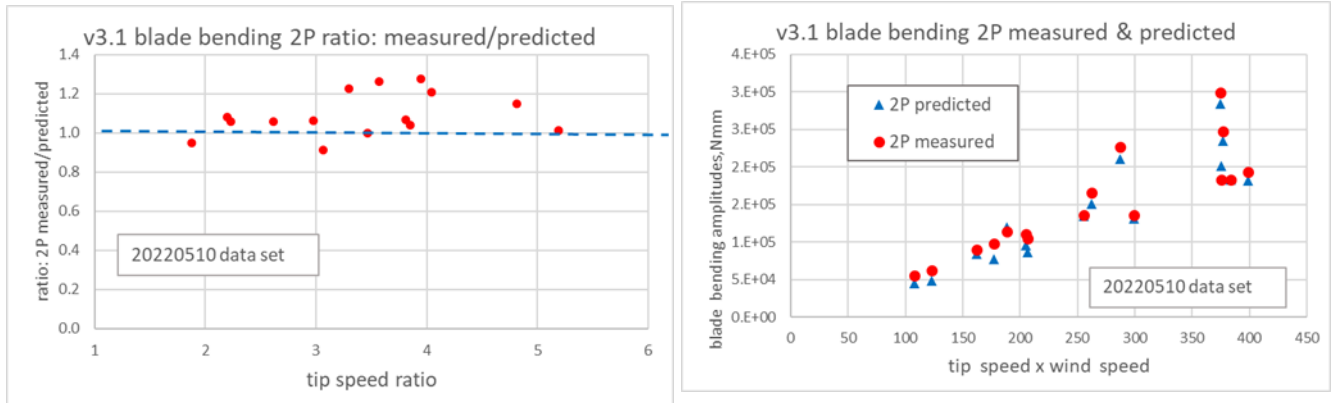
Figure 24. Values and ratios of 2P measured & predicted blade bending

For the 3P harmonic, the measure values are mostly well below the predicted values. See Figure 25
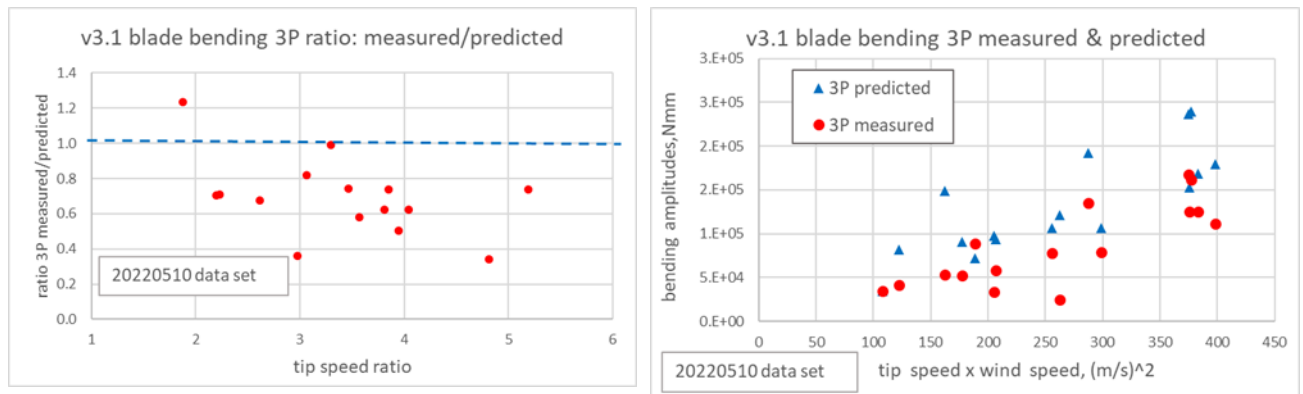
Figure 25. Values and ratio of 3P measured & predicted blade bending

4P measured magnitudes are also less and the predictions are too high at low TSR (Figure 26).
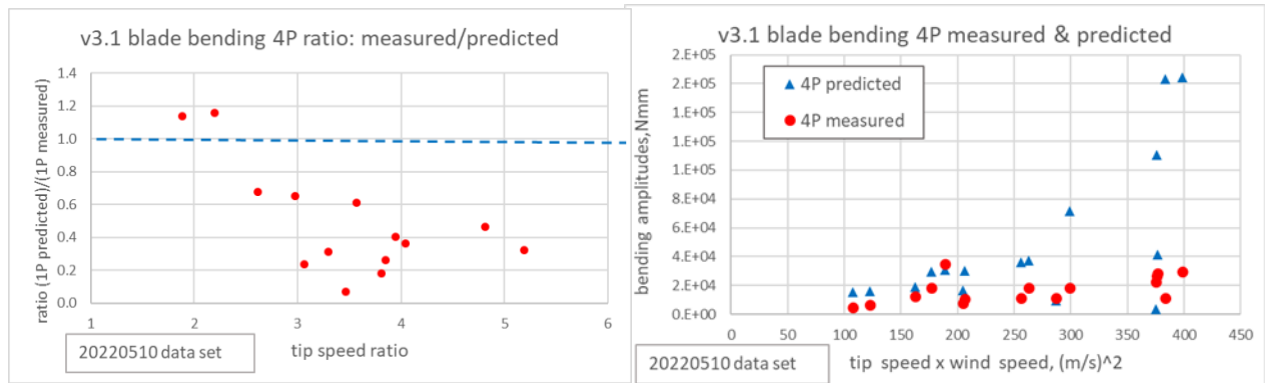
Figure 26. Values and ratios of 4P measured & predicted blade bending

724 N Street, Davis, California 95616 (928) 257-3734

5P measured values are mostly greater than predicted but magnitudes are low (Figure 26).
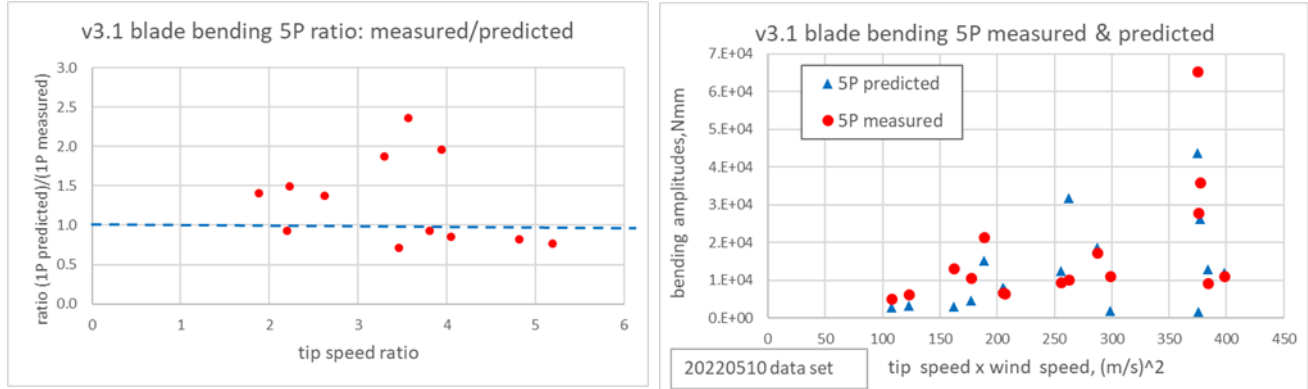
Figure 27. Values and ratios of 5P measured & predicted blade bending

Figure 28 shows the 6P measured values are less than predicted values
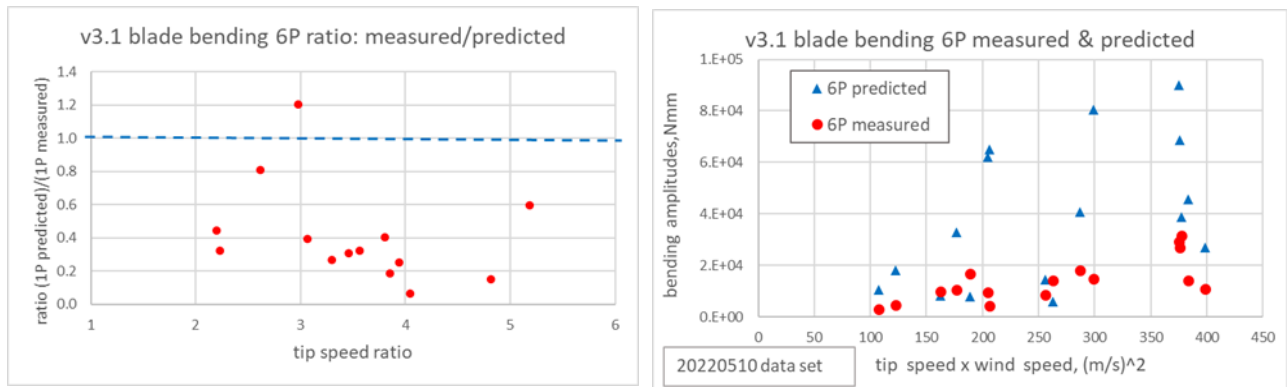
Figure 28. Values and ratios of 6P measured & predicted blade bending

6.6.3   Blade bending vs. azimuth

Field data from the blade bending sensor in the middle of the upper blade indicate that while the response is dominated by the 1P component, there is significant response as high as 6P and 7P in the high wind speed (i.e., low tip speed ratio) data. Examination of the field data around a number of revolutions revealed the nature of this high frequency response, as illustrated in Figure 29 which shows there to be considerable high frequency content although not all of the same phase. Similar behavior was observed in data collected at 46 rpm,
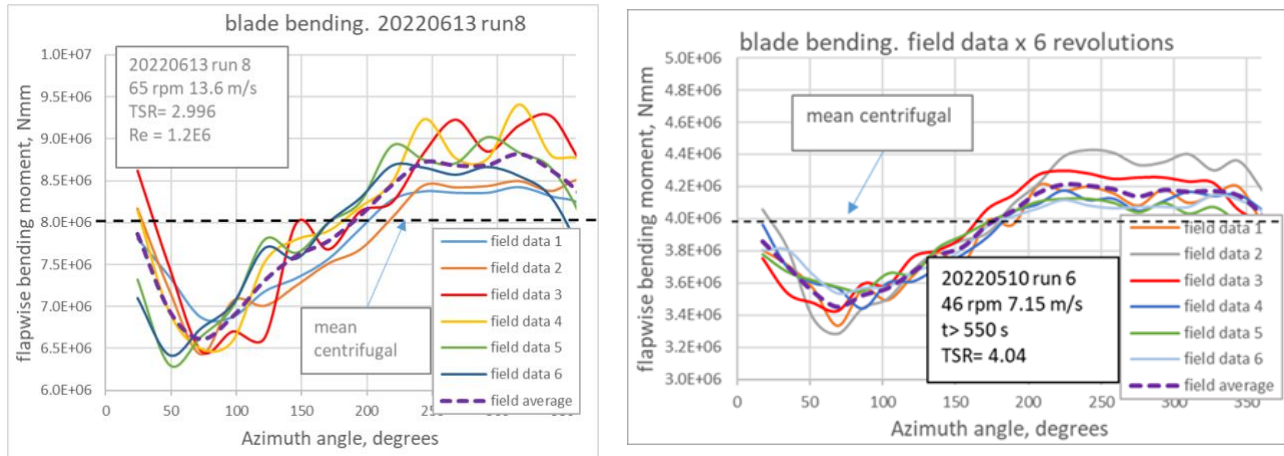
Figure 29. Measured blade bending vs. azimuth for two rotor speeds

A possible contributing cause of this high frequency response was the mast shadow on the downwind blade. The FR4 model was modified to include this effect. The result of this modification is illustrated in Figure 29 which also shows the predicted response with and without dynamic stall (DS).

From Figure 30 it appears that the FR4 predictions without dynamic stall are closer to the measured data, suggesting that the inclusion of dynamic stall may dampen the higher frequency response. Comparison of the harmonic content of the aerodynamic loading and the response indicated there to be considerable amplification at 4P at 65 rpm, some at 5P, and little at 6P. The corresponding modal response showed that the 4P resonance was due to response in real modes 17, 19, and 20 ("blade flap asymmetric").

A similar examination was carried out for the field data from several revolutions at 46 rpm and 7.15 m/s where there is less high-frequency content than from the lower tip speed ratio (Figure 30).
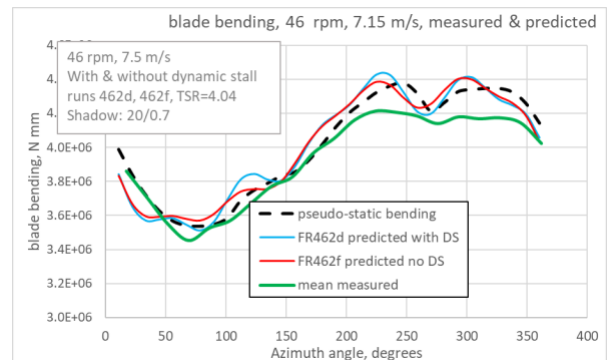
Figure 30. Measured & predicted blade bending vs. azimuth

FR4 blade bending, 65 rpm, 13.6 m/s

65rpm, 13.6 m/s
With & without dynamic stall
runs 474m, 474n
Shadow fraction = 0.5
shadow width =±20°

- pseudo-static bending load
- FR474m response, with DS
- FR474n response, no DS
- average field data
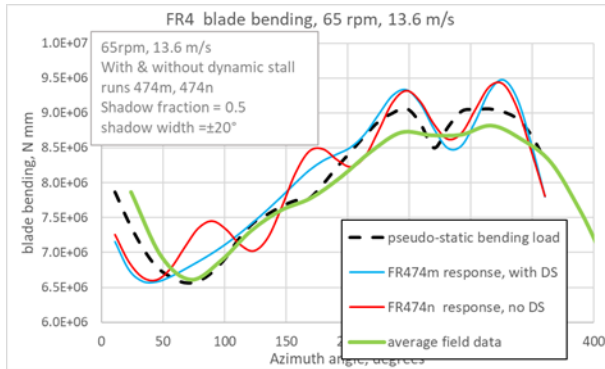
6.7 Arm bending

The out-of-plane bending of the middle arm experiences a peak two times per revolution (once when upwind and once when downwind). The treatment of the predicted value of arm bending was complicated by it being affected by the drag losses from the arm fairing and from the arm-blade connection. An adjustment for these losses was made by observing the power required to motor the rotor in low or zero wind speeds from which it was concluded that the total loss from the rotor at 60 rpm was 17 kW.

6.7.1 Arm bending FFT

Figure 31 shows an FFT of the arm bending signal for two wind speeds at 65 rpm. There is considerable response at higher harmonics such as 5P and 6P at the higher wind speed. There is also suggestion of some resonance at approximately 4.8 Hz.
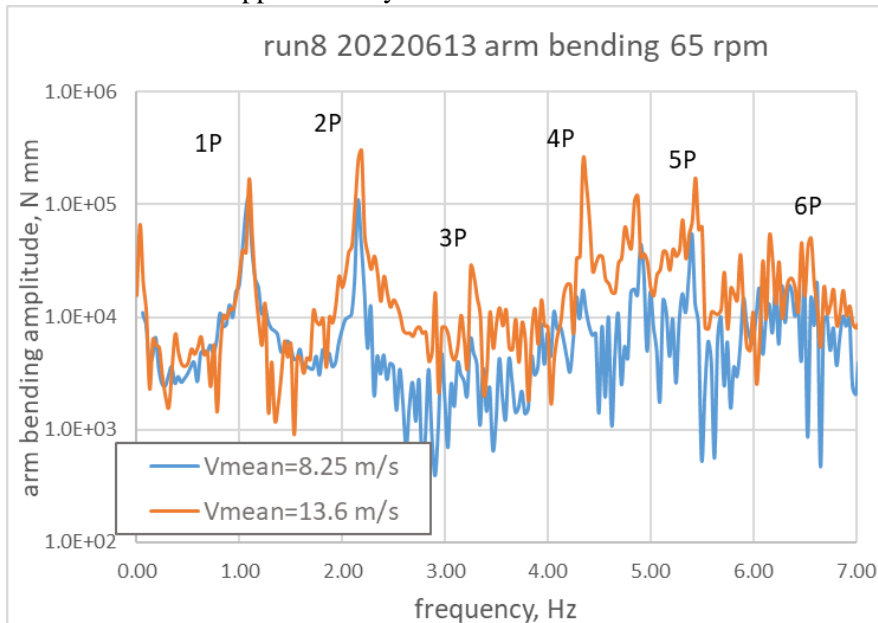
Figure 31. FFT of arm bending at 65 rpm

Figure 32 shows two FFTs from records at 46 rpm. Again there is considerable response at 4P and 5P at the higher wind speed
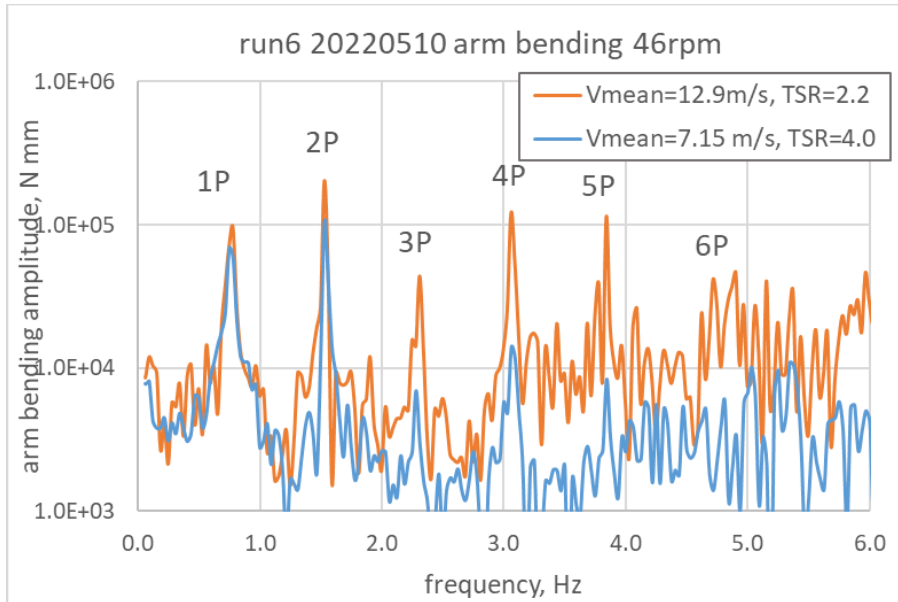
Figure 32. FFT of arm bending at 46 rpm

Both FFTs show the 2P response to be dominant which is to be expected since the arm experiences a positive torque when both upwind and downwind. The 1P signal is a measure of the extent by which the upwind torque is greater than the downwind torque. The higher harmonics may result from similar harmonics observed in the blade bending (and accompanied by corresponding tangential blade forces).

6.7.2   Arm bending, harmonic response

Results of the mean (0P) bending in the arms was not considered reliable due to uncertainties in the offset value used in the calibration. It is, therefore, not reported here.

Figure 33 shows the measured 1P harmonic to be less than the predicted values at low TSR (high wind) conditions and vice versa at high TSR.
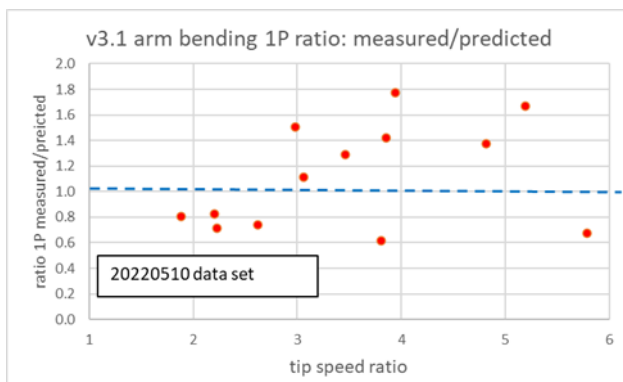
Figure 33. Values & ratios of 1P measured & predicted arm bending

2P is the dominant harmonic for arm bending. Figure 34 shows mixed agreement with the
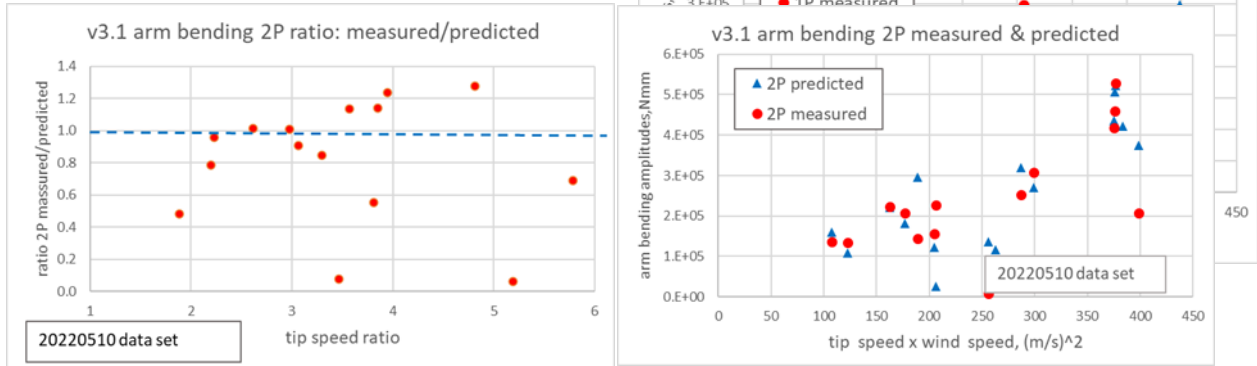
Figure 34. Values & ratios 2P measured & predicted arm bending

predicted values.

Figure 35 shows the corresponding results for the 3P harmonic. All predicted responses are higher than measured which may be due to 3P exciting torsional modes which are well damped in reality. There was unusually high predicted response at 35rpm, 7.3 m/s which may be due to a 3P crossing with 1st torsion which would indeed involve arm bending.
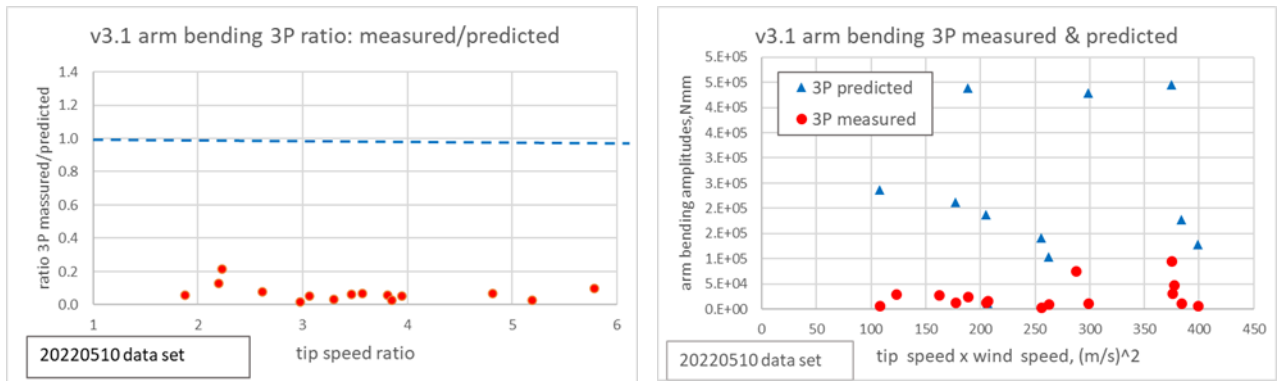
Figure 35. Values & ratios 3P measured & predicted arm bending

Figure 36Figure 36 shows the 4P measured values to be lower than predicted for the entire TSR range. However, the magnitudes are still significant at low TSR.
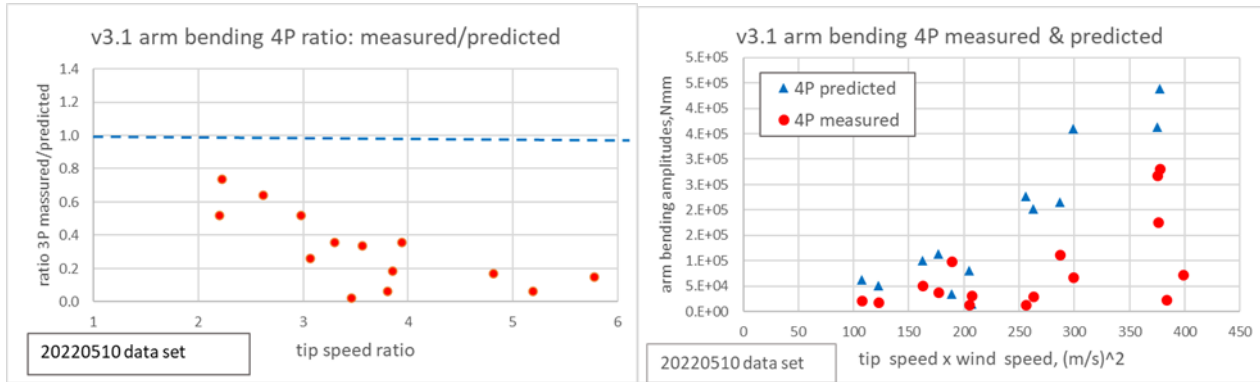
Figure 36. Values & ratios of 4P measured & predicted arm bending

Figure 37 shows the 5P measured harmonic also to be less than predicted but still significant.
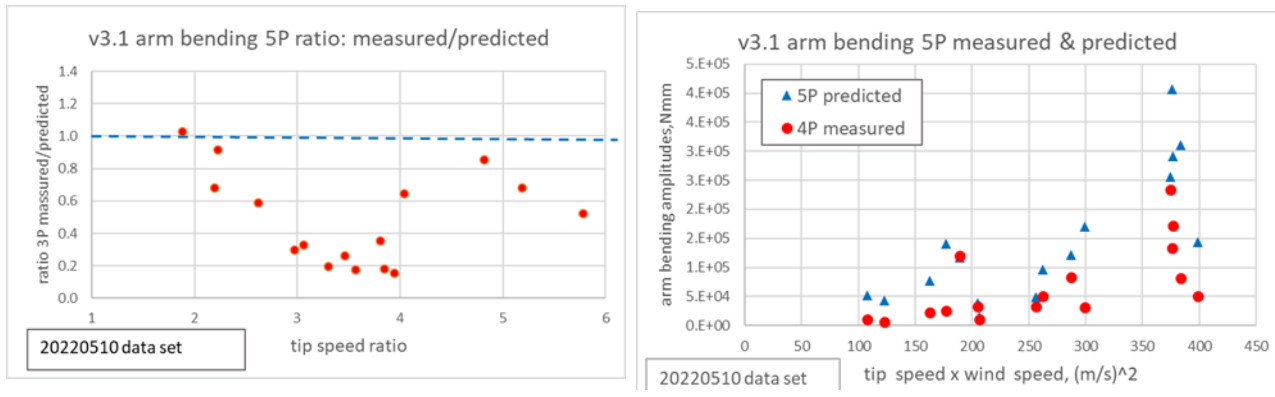
Figure 37. Values & ratios 5P measured & predicted arm bending

Figure 38 shows that at 6P the ratio is reversed: measured values greatly exceed predicted but magnitudes are lower. This could be due to several resonances in the region 4.8-5.0 Hz (in region of 6P at 46 rpm).
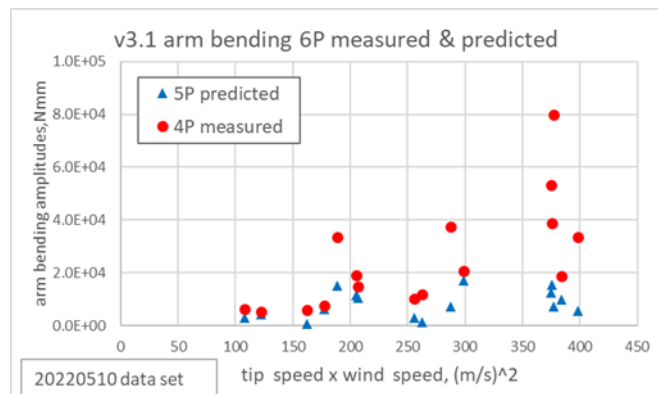
Figure 38 Values & ratios 6P measured & predicted arm bending
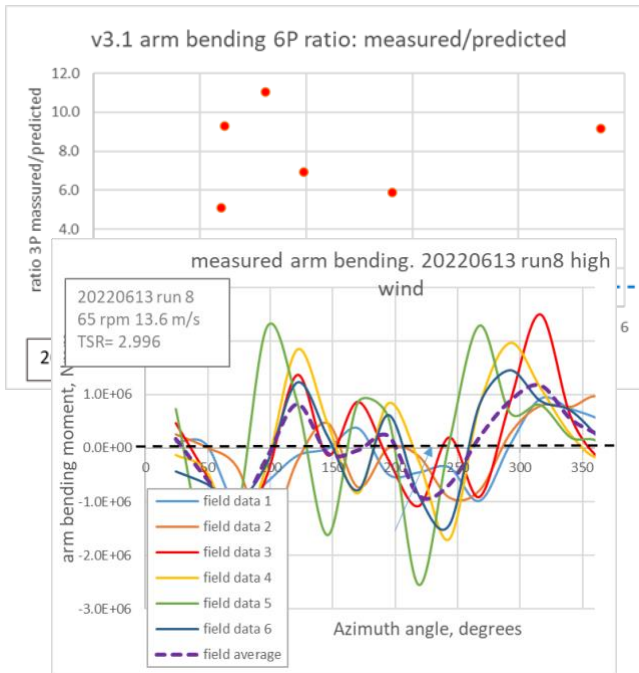
6.7.3   Arm bending vs. azimuth

Figure 39Figure 39 shows measured arm bending over several revolutions at both low and high winds at 65 rpm. The high wind data include more higher harmonics.
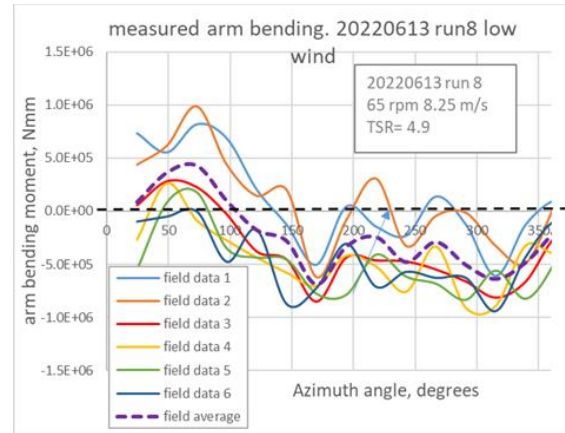
Figure 39. Measured arm bending vs. azimuth,, 65 rpm

Figure 40Figure 40 compares the average of the measured data against predictions with and without the inclusion of dynamic stall.
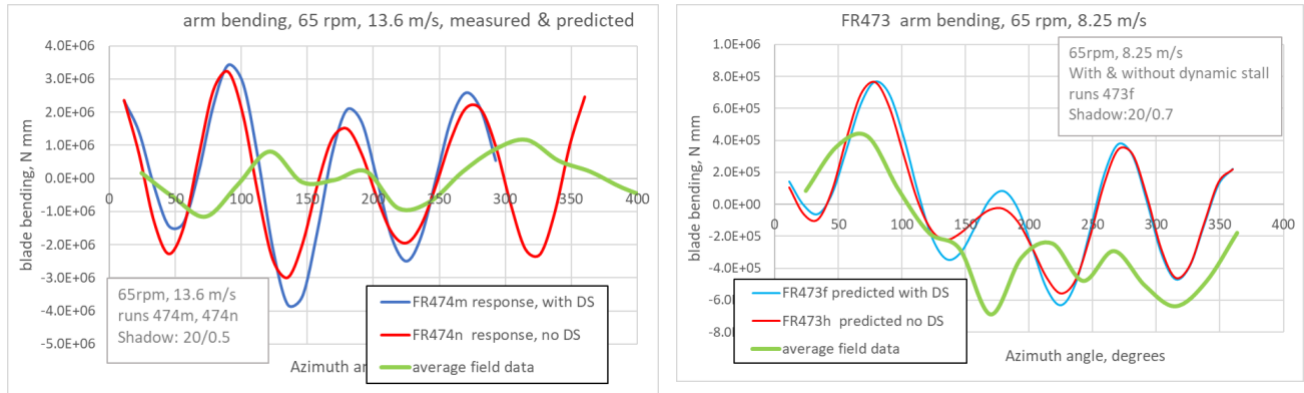
Figure 40. Measured & predicted arm bending vs. azimuth

6.8   Fatigue cycles

The relevant load cycles for determining the fatigue damage to a component is usually carried out with a "rainflow counting" algorithm [8] using NREL's Crunch code. This approach was applied to a number of files of field data for the three instrumented components (the mast, the blade, and the arm bending). 100-second records were selected when the wind speed and response were fairly constant. The resulting histograms of fatigue cycles were compared with those derived from the corresponding FR4 predictions using the LIFE82 code [9].

The LIFE code was first developed at Sandia National Laboratory in the 1980s as part of the program researching the curved-blade Darrieus rotor VAWT. At that time the structural analysis codes were limited to the frequency response at the rotor harmonics (rather than the time-step integration methods now used on most HAWTs). In order to simulate the atmospheric turbulence and variation in the magnitude of the harmonic responses, the LIFE code applied a Weibull distribution to the magnitude of those cycles. The same approach is used in the LIFE82 developed by Wind Harvest.

6.8.1   Fatigue cycles – mast bending

Figure 41Figure 41 shows that the mast bending response is dominated by the 1P harmonic at all wind speeds.
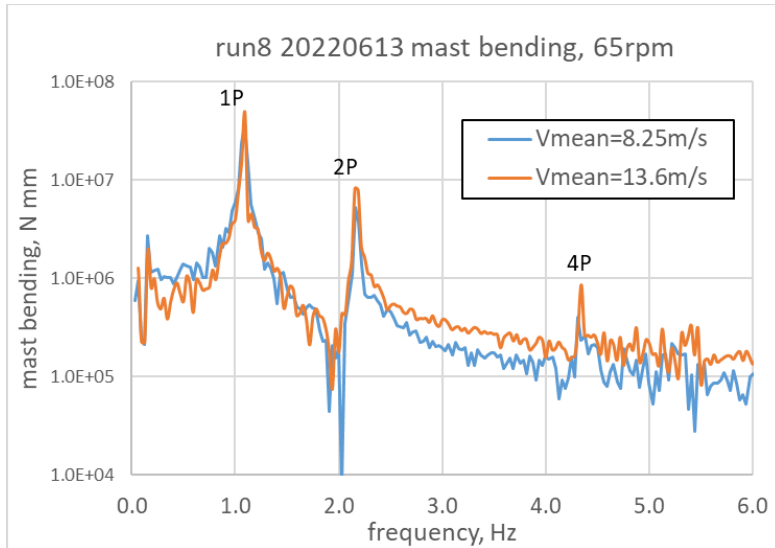
Figure 41. FFT of mast bending, 65 rpm

Using the standard deviation from the appropriate FR4 simulation (FR480a), and a Weibull shape factor (k) of 10, Figure 42Figure 42 shows very good agreement between the LIFE results and the measured rainflow-counted fatigue cycles. This is consistent with Figure 15 which shows close agreement between the measured and predicted 1P amplitudes at all tip speed ratios.
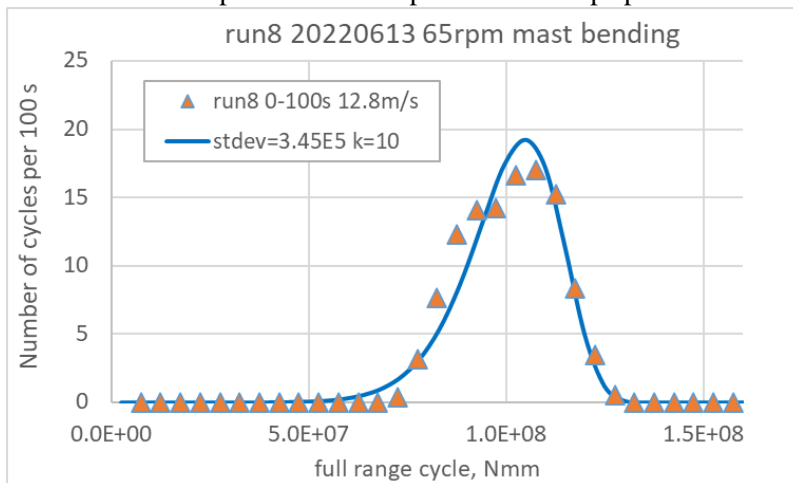
Figure 42. Measured and predicted fatigue cycles, mast bending

6.8.2   Fatigue cycles – blade bending

The blade bending response is also dominated by the 1P harmonic, as shown in Figure 43Figure 43 but some higher harmonics are also present especially at high wind speeds (lower tip speed ratios).
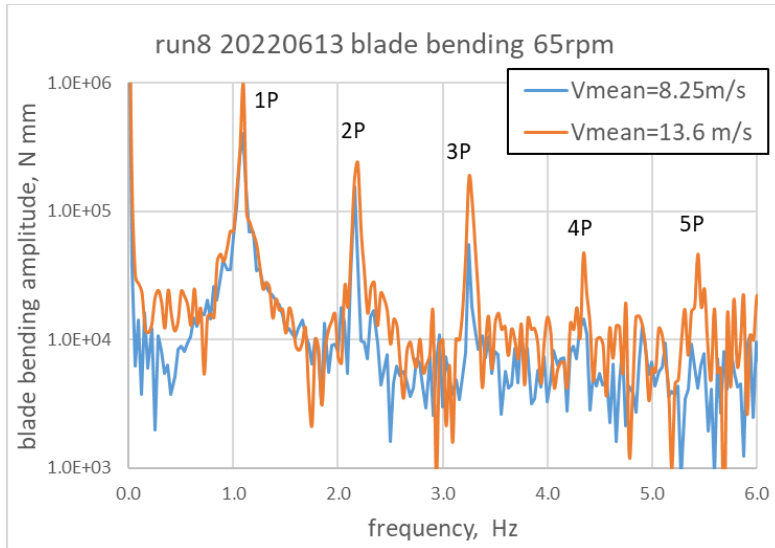
Figure 43. measured FFT of blade bending, run 8 2020613

A comparison of the measured rainflow cycles and the prediction from the FR4 simulation is shown in Figure 44. The predicted ranges are 10-15% higher than the measured values which is consistent with the ratio of the 1P magnitudes in Figure 23.
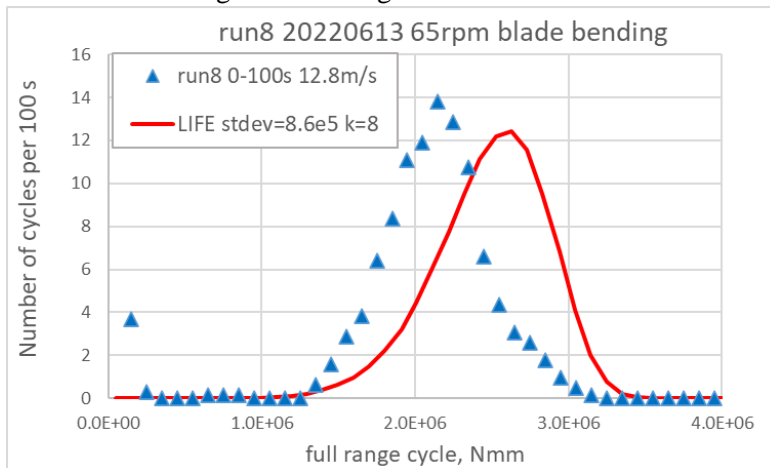
Figure 44. Measured and predicted blade bending fatigue cycles

6.8.3   fatigue cycles – arm bending

The frequency from the arm bending shows considerable response at the higher harmonics (4P and 5P) especially at high wind speeds or low tip speed ratios. This complicates the distribution of rainflow-counted cycles from the field data which is no longer a single peak.

The FR4 code overpredicts the 3P and 4P response at some rotor speeds due to resonances which are not present in the field data. Better agreement can be reached by adding damping to the higher modes of the

rotor structure. This is illustrated in Figure 45 where, without added damping, there could be a resonance at 4P at 65 rpm.
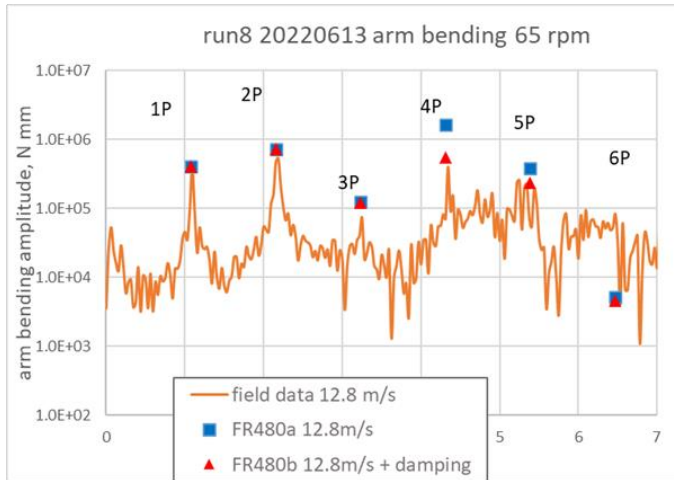
Figure 45.FFT of measured arm bending and predicted harmonic amplitudes, 65 rpm

The distribution of rainflow-counted fatigue cycles is very broad for this condition (see Figure 46) and cannot be fully duplicated by a single Weibull distribution. However, it is necessary only for the LIFE82 code to duplicate the high-amplitude tail of the distribution since those cycles lead to the most fatigue damage. In addition to having to choose a lower shape factor for the Weibull distribution to obtain a good match with the field data, it is also necessary to estimate an effective frequency. For signals, such as the mast bending, which are dominated by the 1P harmonic, that frequency is clear. If higher harmonics are significant, then the choice of one frequency is not clear.
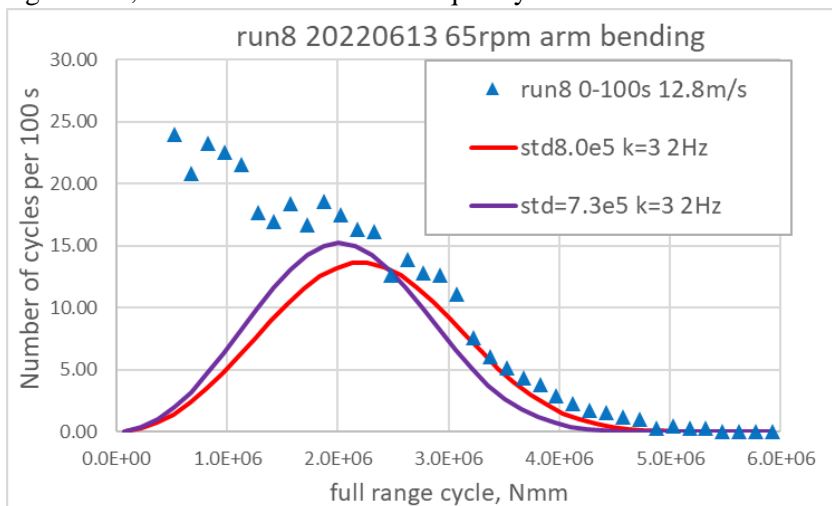
Figure 46. Measured and predicted fatigue cycles, arm bending, high wind speed 65 rpm

Figure 47Figure 47 shows another arm bending FFT at a low tip speed ratio which includes higher harmonics. At 50 rpm there was some resonance at 3P in the FR4 model which, when damping was added, led to better agreement with the field data.
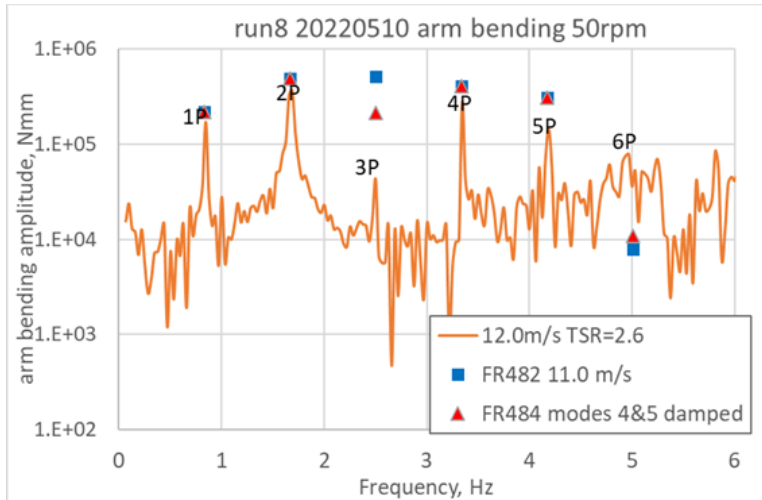
Figure 47. FFT of measured arm bending and predicted harmonic amplitudes, 50 rpm
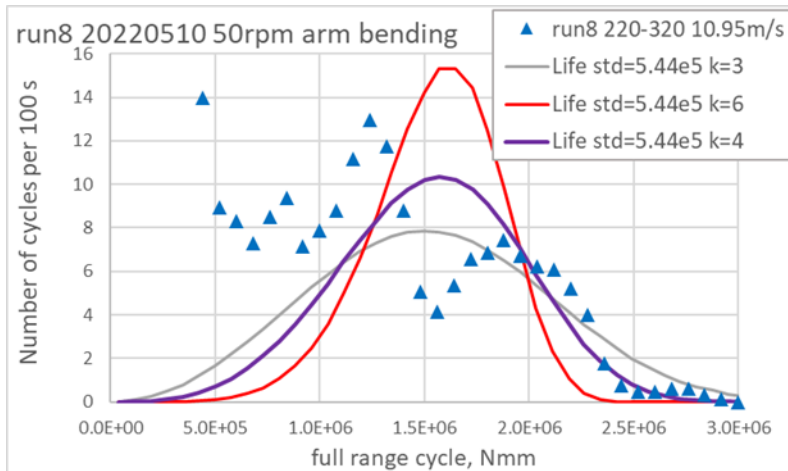
Figure 48. Rainflow fatigue cycles and LIFE distribution, arm bending, 50 rpm,10.9 m/s

Figure 49 and Figure 50 present corresponding results for a lower wind speed at 50 rpm. There are no higher harmonics present in the field data, but some are predicted from the FR4 model which justifies adding damping to the model for those higher modes. A Weibull shape factor of k=4 appears to best fit the tail of the rainflow distribution.
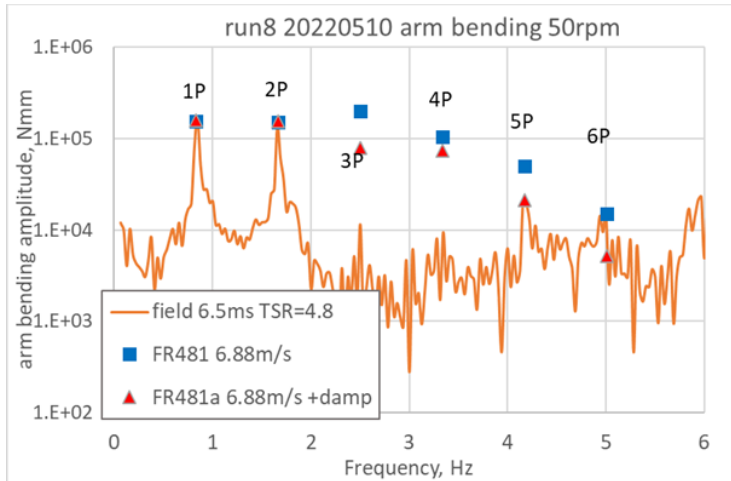
Figure 49. FFT of arm bending and predicted harmonics, 50 rpm, 6.5 m/s
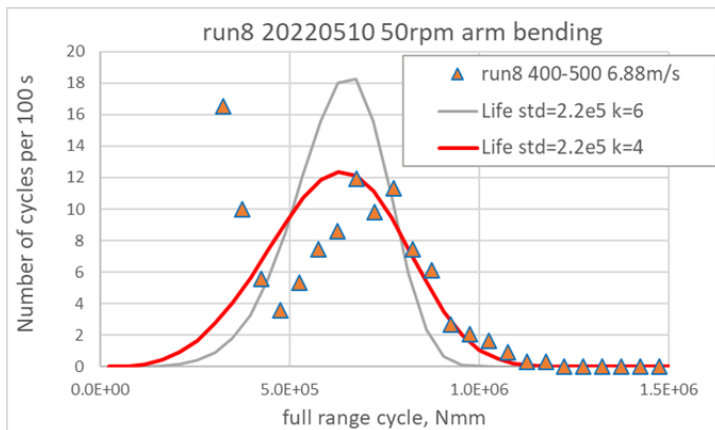
Figure 50. Rainflow counted fatigue cycles and LIFE distributions, 50 rpm, 6.8 m/s

6.9   Aerodynamic performance

Early in the program it was decided to lower (derate) the maximum electrical power of the system from 65 kW to approximately 50 kW. This was done to avoid possible overloading the generator. It was achieved by lowering the rotor speed in high winds.

Figure 51 compares the predicted electrical power performance with wind speed as well as measured values from two sets of field data during which the turbine was operated in "variable speed mode". The estimated values were obtained from the CACTUS code [12] using an air density of 1.05 kg/m^3 which was estimated to be the typical density at the test site. The rotor speeds used in the CACTUS simulations corresponded to the average recorded during the "2023.04.04" data set. The CACTUS code supplied the aerodynamic power without any adjustment for drag and other losses. Those losses were estimated with the help of earlier tests on the spinning rotor in zero wind speed conditions from which the

drag losses were determined to be 17 kW at a rotor speed of 60 rpm. Drag losses were considered to be proportional to the cube of the wind speed and were adjusted accordingly. Mechanical and electrical losses were estimated to be 7% of the rotor power.

The field data was analyzed by a binning code that used 1-minute averaged windspeeds and electrical power. Both sets of field data in Figure 51 are shown to be close to the predicted "derated" power curve.
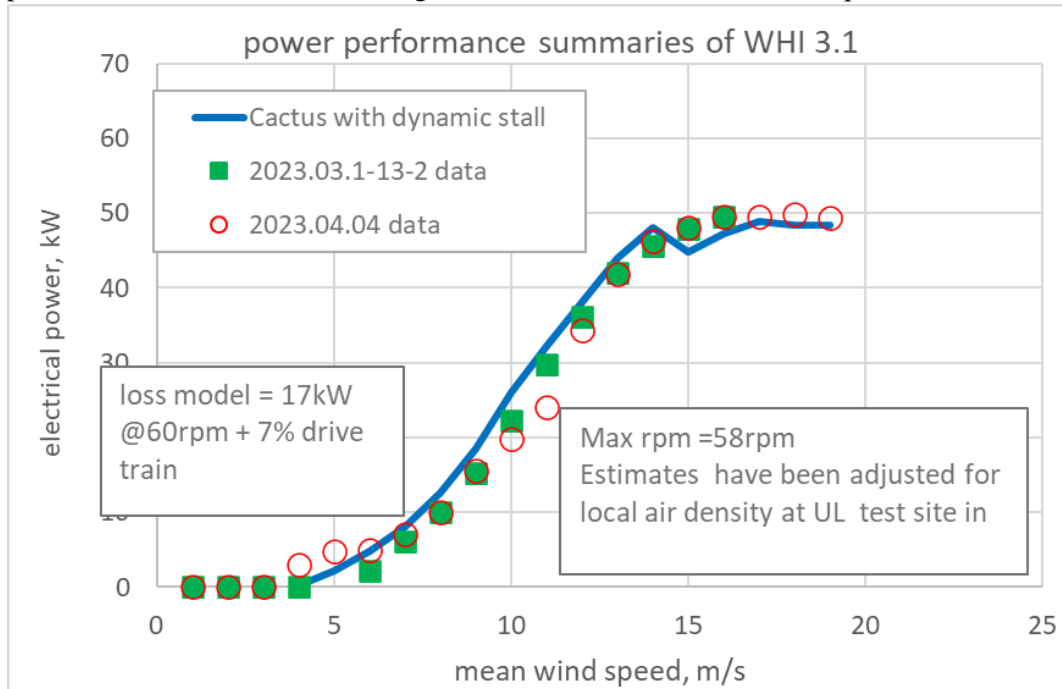
Figure 51. Estimated power performance vs. measured binned data. 58rpm max.

Figure 52 shows the same field data expressed as a power coefficient and plotted against the tip speed ratio. The other lines are estimated values, again starting with the CACTUS code and using the same loss model as described above. The pairs of estimates were obtained at two rotor speeds, 35 and 60 rpm, since most of the operation occurred within those bounds. The maximum electrical power coefficient appears between 0.25 and 0.3 which agrees well with predictions,
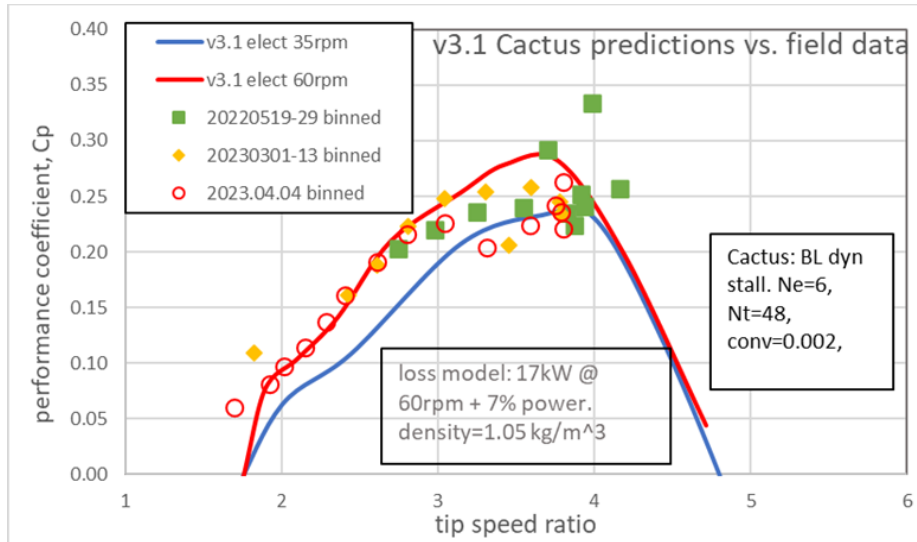
Figure 52. Predicted & measured tip speed ratio vs. performance coefficient

6.10 Dynamic stall

The effect of dynamic stall is to delay the occurrence of stall and is dependent on the rate of change of the angle of attack. There are several empirical models for this behavior [10, 11]; the one included in the FR4 code was the Gormont stall model [10]. Its effect can be determined by running the code both with and without the dynamic stall option included. Dynamic stall will occur only in those cases where the angle of attack exceeds the stall angle which is in the range of 12 to 14 degrees. This corresponds approximately to tip speed ratios less than 3.5.

Figure 53 shows an example of the predicted effect of dynamic stall on the blade bending over one revolution. The tip speed ratio is 2.2 which implies considerable stall. As well as a greater range over one revolution, the bending with dynamic stall shows more high frequency content which is consistent with detailed frequency response analysis.

The field bending data included in Figure 53 is an average over several revolutions. Individual revolutions exhibited considerable high frequency content (such as 4P and 6P).
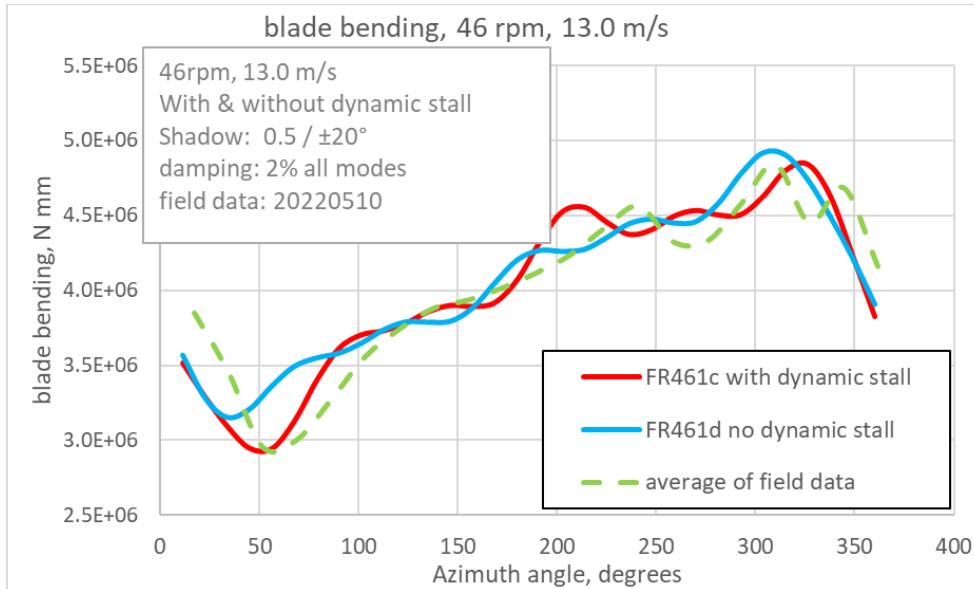
Figure 53. Predicted blade bending with & without dynamic stall vs. field data

Dynamic stall also has a significant effect on the rotor performance as shown in Figure 54. The measured performance agrees closely with the predictions that include dynamic stall, thus confirming the presence of this phenomenon.

Figure 54. Electrical performance with and without dynamic stall

6.11 Response at higher harmonics

One noticeable result from the analysis of the data was the presence of higher harmonics (4P, 5P, and 6P) in some of the responses. This is apparent in, for example, Figure 22 and Figure 32. The possible causes of this response 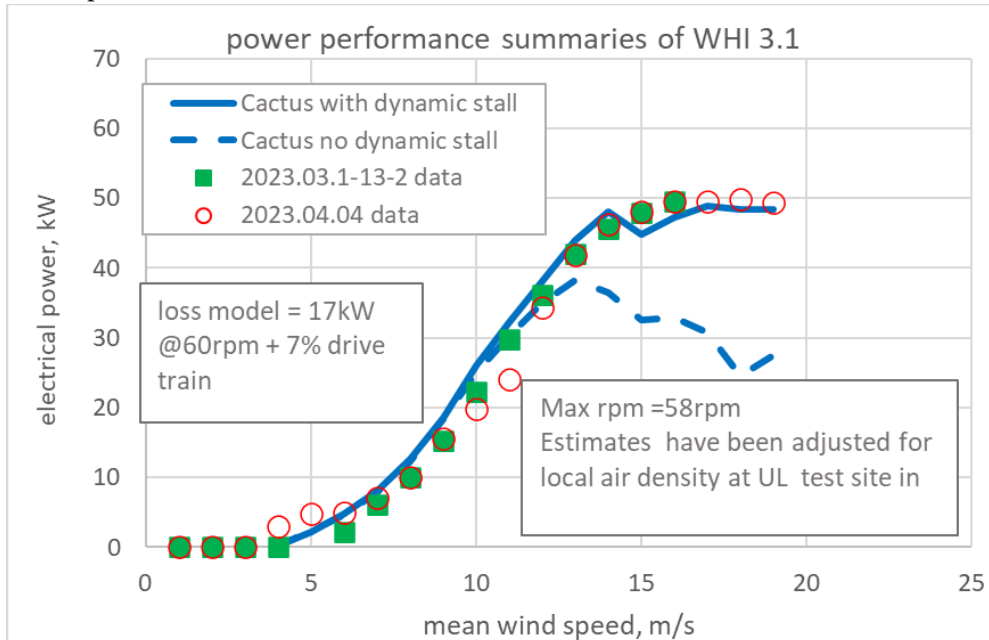were considered to be the sharp stall that can occur under some conditions and also the passage of the blade through the shadow downwind of the central mast.

The DMST routine in the FR4 code was modified to include a downwind shadow that could be turned on or off and with an adjustable severity. It was also modified to include harmonic responses up to 6P. An example of the effect of including a mast shadow is shown in Figure 55.
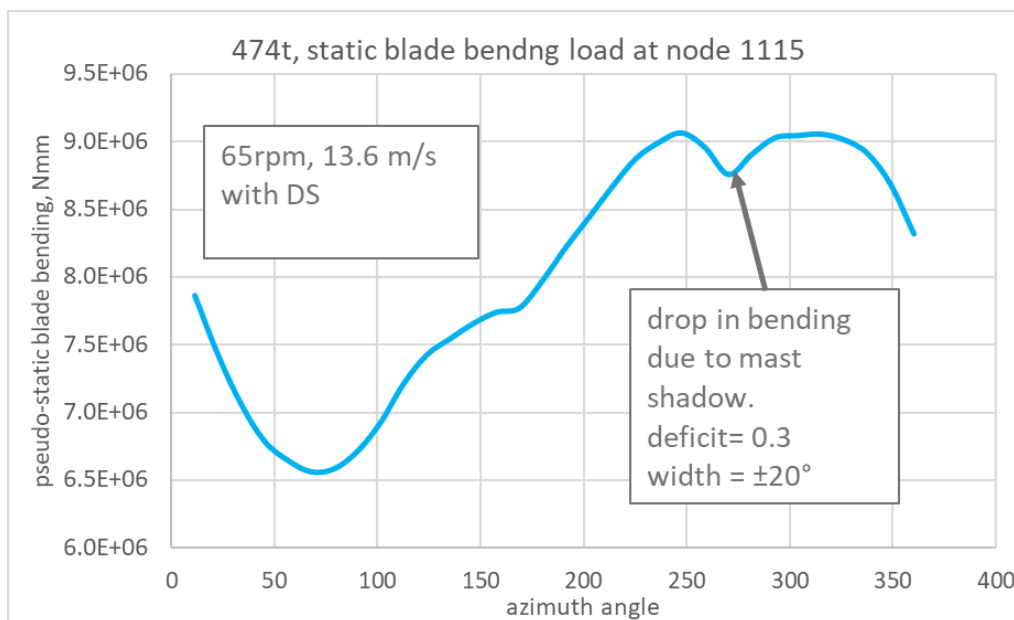
Figure 55. Example of mast shadow effect on blade loading.

7   Summary and Conclusions

This report has brought together much of the structural and performance data from the operation of the Wind Harvest 3.1. The response at three of the sensors was examined in detail (the lower mast bending, lower mast torque, the bending in the middle of the upper blade, and the out-of-plane bending of the middle arm). In general, the predictions of the mean and harmonic values for the three responses are in good or acceptable agreement with the field data.

- The mast bending is dominated by the 1P harmonic which is in good agreement with the predicted amplitude across a full range of tip speed ratios.
- The mast torque was predicted to be dominated by a 3P peak. However, the field result show larger 1P and 2P harmonics which suggests that either the gauges are misaligned or that the processing is incorrect.

- The blade bending signal contained considerable components from higher harmonics (4P and higher) especially at low tip speeds. These are probably due to the regular sharp stalling action and also to the passage of the downwind blade through the mast shadow.
- The agreement between the predicted and measured 1P and 2P blade bending harmonic amplitudes was good at all tip speed ratios. For the 4P and 6P harmonics, the code over-predicted the amplitudes especially at high tip speed ratios while the agreement was better for 5P.
- Field data confirmed that the arm bending response is dominated by the 2P harmonic. However, as well as a strong 1P component, there are substantial 4P, 5P, and 6P contributions, especially at low tip speed ratios. These can be related to stall and mast shadow effects.
- While the FR4 model showed some resonance in higher modes at 46 rpm and 65 rpm due to 4P and 6P excitation, there was little field confirmation of such response. This supported including up to 20% damping in the higher natural modes in the model.
- In most of the field data there was considerable vertical wind shear and a wind shear exponent of 0.16 was considered appropriate. In general, this increased the magnitude of the predicted responses.
- The measured electrical power over a range from 5 m/s to 19 m/s agreed closely with the estimates adjusted for air density, parasitic drag, and drive train losses.

8   References

1. Sutherland HJ, Berg DE, Ashwill TD. A Retrospective of VAWT Technology, *Sandia National Laboratories*; SAND2012-0304.
2. Vertical Axis Wind Turbines, The History of the DOE Program, http://windandwaterpower.sandia.gov.
3. Malcolm, D.J., Validation of the EOLE suite of codes for the structural response of vertical axis wind turbines, Wind Harvest International, April 2016
4. Malcolm, D.J., Theoretical basis of the Forced Response codes for Vertical Axis Wind Turbines, Wind Harvest International, December 2021
5. Malcolm, D.J., "The response of two- and three-bladed vertical axis wind turbines," Wind Energy, 2019-19.
6. Malcolm, D.J. "Structural response of 34-m Darrieus rotor to turbulent winds", Journal of Aerospace Engineering, ASCE, Vol. 6, No. 1, 1993.
7. Malcolm, D.J., "Dynamic response of a Darrieus rotor wind turbine to turbulent flow", Engineering Structures, Vol. 10, April 1988
8. Downing, S.D., Socie, D.F. (1982). "Simple rainflow counting algorithms". International Journal of Fatigue. **4** (1): 31–40.
9. Outline of LIFE81.f95: update of Life75 for calculating fatigue life of VAWT components, Wind Harvest International, David Malcolm, August 2021
10. Gormont, Ronald E. (1973-05-01). A Mathematical Model of Unsteady Aerodynamics and Radial Flow for Application to Helicopter Rotors from the original on June 24, 2021
11. Leishman, J. G.; Beddoes, T. S. (1989-07-01). "A Semi-Empirical Model for Dynamic Stall". *Journal of the American Helicopter Society*. **34** (3): 3–17.

12. Murray, J.C., Barone, M., Development of CACTUS, a wind and marine turbine performance simulation code. 49th AIAA Aerospace Sciences Meeting, Orlando, FL Jan. 2022

Appendix A. Field Data Collected

The table below lists the data collected and used in this report.

date	Name of file	comment
2022.03.04	RUN1 30RPM-6.7msDM.xlsx	
	RUN2 35RPM-7.5msDM.xlsx	
	run7-9-12 fieldData_extractOlaDM.docx	
	RUN11 45RPM-9.4msDM.xlsx	
2022.03.14	RUN1 20220314 46RPM-12.4msDM.xlsx	
	RUN10 20220314 57RPM-15.9msDM.xlsx	
	RUN9 20220314 62RPM-14.6msRnflwDM.xlsx	
2022.05.10	run1 20220510 30rpm DM2.xlsm	
	run2 20220510 35rpm DM2.xlsm	
	run3 20220510 40rpm DM2.xlsm	
	run6 20220510 46rpm DM2.xlsm	
	run8 20220510 50rpm DM2.xlsm	
	run10 20220510 54rpm DM2.xlsm	
	run12 20220510 58rpm DM2.xlsm	
	run14 20220510 62rpm DM2.xlsm	
	run15 20220510 emergencyStopDM.xlsm	
2022.05.17	12H VSA Endurance Test DM.xlsx	
2022.05.19	24H VSA Endurance Test +DMbins.xlsx	
2022.06.13	run1 20220613 30rpm DM.xlsm	
	run3 20220613 40rpm DM.xlsm	
	run6 20220613 55rpm DM.xlsm	
	run7 20220613 60rpm DM.xlsm	
	run8 20220613 65rpm DM2.xlsm	
2023.03.01	March 1st - 13th VSA Data Bin-dm.xlsx	
2023.03.21	March 21st 2023 VSA.xlsx	??
2023.04.04	April 4th, 2023_VSA Data Bin.xlsx	